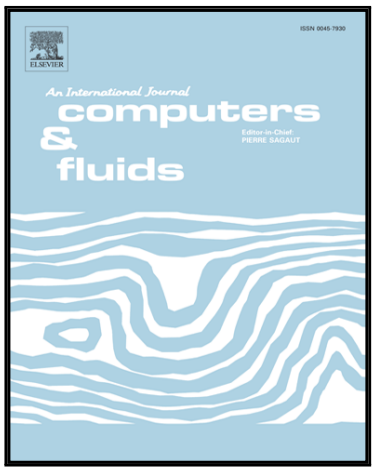

On the influence of modelling choices on combustion in narrow channels

X. Kang, R.J. Gollan, P.A. Jacobs, A. Veeraragavan

PII: S0045-7930(16)30372-3
DOI: 10.1016/j.compfluid.2016.11.017
Reference: CAF 3338

To appear in: *Computers and Fluids*

Received date: 13 May 2016
Revised date: 25 August 2016
Accepted date: 26 November 2016

Please cite this article as: X. Kang, R.J. Gollan, P.A. Jacobs, A. Veeraragavan, On the influence of modelling choices on combustion in narrow channels, *Computers and Fluids* (2016), doi: 10.1016/j.compfluid.2016.11.017

Highlights

- Systematic analysis of modelling choices pertaining to micro-flames is presented
- Grid Converence Index (GCI) is used to determine appropriate mesh-density
- Influence of different 'ignition methods' on flame initiation is investigated
- Recommendations are made on appropriate modelling choices for micro-flames

On the influence of modelling choices on combustion in narrow channels

X. Kang, R. J. Gollan, P. A. Jacobs, A. Veeraragavan*

School of Mechanical & Mining Engineering,
The University of Queensland, QLD 4072, Australia

Abstract

This paper examines the effect of modelling choices on the numerical simulation of premixed methane/air combustion in narrow channels. Knowledge on standard and well-accepted numerical methods in literature are collected in a cohesive document. The less well-established modelling choices have been thoroughly evaluated and discussed. A systematic method of computing the grid convergence index (GCI) has been presented for refining the computational grid. Two types of inflow boundary conditions have been tested and compared in terms of their wave-damping characteristics. The effect of different reaction schemes on simulation results have been examined and an appropriate mechanism (DRM-19) has been selected. Various types of ignition strategies to initiate the flame have been tested and compared. The transient ignition process which has not been discussed extensively in existing literature has been quantitatively described in this paper.

Keywords:
Micro/mesoscale combustion, Numerical Modelling, Boundary conditions, Grid Convergence Index, Ignition Methods

1. Introduction

Micro/mesoscale combustion has received research impetus in the past two decades for both fundamental understanding and targeted application in portable power systems and

*Corresponding author
Email address: anandv@uq.edu.au (A. Veeraragavan)

propulsion systems for small scale rockets. Compared to traditional electrochemical batteries, micro/mesoscale combustion takes advantage of the considerably higher energy densities (45 vs 0.6 MJ/kg) and instant rechargeability, thereby leading to fewer logistical issues [1]. Fundamentally, micro/mesoscale-combustion can be viewed as combustion in narrow passages or ducts typically on the order of the flame thickness, with strong thermal coupling between the combustor's structure and the flow. At these scales, combustion poses challenging problems. For example, the large combustor surface heat losses and short flow residence times can potentially induce flame instabilities or even flame quenching [2]. In order to make micro/mesoscale combustion a viable technology, it is critical to comprehensively understand its fundamental aspects and tackle the challenges identified.

Past work on experimental studies established [3] and enhanced [4] operational regimes/ flame stability limits, and demonstrated a range of interesting flame features such as flames with repetitive extinction and ignition (FREI) [5] as well as various flame patterns [6].

However, experimental works have inherent difficulties in obtaining spatially resolved measurements on a small scale. Similarly, theoretical models can also be used to understand the underlying microcombustor physics regarding heat recirculation [7, 8], however, their results can only be interpreted in a qualitative sense as they use several simplifications and assumptions in order to develop a closed-form solution. On the other hand, numerical models do not make such assumptions and are capable of quantitatively revealing detailed physical features and can therefore be used as a reliable tool that develops the understanding of current configurations and supports the design of future systems. Some past numerical simulations using a steady-state [9–15] or transient [5, 16–22] model were conducted, with a focus on the flame stabilities and flame dynamics.

In the realm of simulation works, some numerical methods/modelling choices are considered as well-accepted standards in the micro/mesoscale combustion community. For instance:

- Since the characteristic length scale for micro/mesoscale combustion is on the order of sub-millimetres to several millimetres, the Reynolds number is relatively small. The

flow condition thereby typically remains in the laminar regime. It should also be noted that some numerical studies [23, 24] used turbulence models to simulate micro-combustor with complex geometries (cavities/bluff bodies) since the burning velocities of those micro-flames were dramatically enhanced, leading to the Reynolds number exceeding the critical value.

- Under low Reynolds number conditions, molecular mass diffusion becomes a primary mechanism for mixing [25]. The mixture Lewis number is found to have an important influence on the formation of different flame modes [26]. Therefore, an appropriate mass diffusion model is needed.

- On the other hand, the "small" characteristic dimensions are still significantly larger than the molecular mean free path [2]. The Knudsen number (defined as the ratio of mean free path to the characteristic length) is adequately small such that continuum theory is still a good assumption.

- Analogous to combustion at a conventional scale, micro/mesoscale combustion has also considerable effects on the density of the gas due to the chemical heat release. The low speed flows at small scales should still be regarded as compressible.

However, as per the authors' knowledge, there are still some modelling techniques/choices which are less well-established or need more discussion. For example, if the reason for the choice of a particular model has not been explained in detail. Table 1 has summarised the simulation choices in past studies with our remarks. It sets the scope of this study. In the author's opinions, the less-justified modelling choices include considerations on the truncation error choice (related to the grid refinement study), the means for setting the boundary conditions, selection for appropriate reaction schemes and strategies for initialising simulations.

In this paper, the authors have developed, through investigation, a set of modelling techniques that gives guidelines and best practices for performing the micro-flame simulations. After an introduction to our in-house numerical solver in Section 2, the choices of

Table 1: Summary of simulation choices for micro-flame numerical studies.

Simulation choices	Commonly applied methods in literature	Well established ? or subject to debate
Steady-state/ transient	The choice depending on the interest of research	Transient flow (more general) is studied in this work
Laminar/turbulent	Without turbulence model for most cases	Yes
Thermodynamic properties (species)	Piecewise polynomial curve fitting as a function of temperature	Yes
Thermodynamic properties (mixture)	Mass fraction weighted sum of each species	Yes
Thermal transport properties (species)	Piecewise curve fitting or using kinetic theory	Yes
Thermal transport properties (mixture)	With appropriate mixing rules	Yes
Mass diffusion	Mixture-averaged or multicomponent based on kinetic theory	Yes
Chemical kinetics	Finite-rate chemistry with various reaction schemes used	The choice of an appropriate scheme needs discussion
Boundary conditions	Velocity inlet Fixed pressure outlet No-slip wall	More discussions in this work: e.g. a mass flux inflow BC should be used instead of velocity inflow
Initiation strategy	Several methods used with limited details	Flame ignition process needs quantitative study
Grid refinement	Usually determined with visual observations	Requiring for a more rigorous and systematic method

the above-mentioned modelling approaches will be thoroughly considered and studied for a premixed methane/air flame in a narrow channel. The authors wish to share the findings as recommendations for others.

2. Numerical solver

Figure 1 shows the two-dimensional (2D) computational domain between two parallel plates for the numerical model. The channel length (L) is 6 mm and channel height (H) is 0.6 mm, which forms a length-to-height aspect ratio of $L/h = 10$.

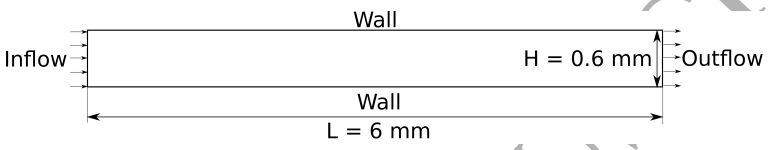

Figure 1: Computational domain of the planar micro-channel.

As mentioned earlier, the premixed methane/air flame propagation in this 2D, planar micro-channel is numerically studied using our in-house code, Eilmer [27], which solves for transient, compressible, reacting flows. A cell-centred, finite volume method is employed for the discretisation of the governing equations.

The solver is based on the integrated Navier-Stokes equations over a control volume, which can be written as

$$\frac{\partial}{\partial t}\int_V U dV = -\oint_S \left(\overline{F}_i - \overline{F}_v\right)\cdot \hat{n}\; dA + \int_V Q dV \;, \tag{1}$$

where V is the control volume and S is the bounding surface. The symbol $\hat{n}$ represents the outward-facing unit normal of the bounding surface. U, $\overline{F}_i$, $\overline{F}_v$ and Q are the conserved quantities, inviscid fluxes, viscous fluxes and source terms respectively.

A detailed description of the solver and governing equations is given in the article by Gollan and Jacobs [27]. The key governing equations are repeated here for completeness. For a two-dimensional model, the array of conserved quantities U can be written as a summation of density, x-momentum per volume, y-momentum per volume, total energy per volume and mass density of species s:

$$U = \begin{bmatrix} \rho \\ \rho u_x \\ \rho u_y \\ \rho E \\ \rho Y_s \end{bmatrix} . \tag{2}$$

where u_x and u_y are the Cartesian velocity components, E is the specific total energy of the gas mixture (a sum of the internal energy and kinetic energy: $E = e + \frac{1}{2}(u_x^2 + u_y^2)$) and Y_s is the mass fraction of species s.

The inviscid fluxes $\overline{F}_i$ are expressed as

$$\overline{F}_i = \begin{bmatrix} \rho u_x \\ \rho u_x^2 + p \\ \rho u_y u_x \\ \rho E u_x + p u_x \\ \rho Y_s u_x \end{bmatrix} \hat{i} + \begin{bmatrix} \rho u_y \\ \rho u_x u_y \\ \rho u_y^2 + p \\ \rho E u_y + p u_y \\ \rho Y_s u_y \end{bmatrix} \hat{j} , \tag{3}$$

where p is the static pressure.

The viscous fluxes $\overline{F}_v$ are expressed as

$$\overline{F}_v = \begin{bmatrix} 0 \\ \tau_{xx} \\ \tau_{yx} \\ \tau_{xx} u_x + \tau_{yx} u_y + q_x \\ J_{x,s} \end{bmatrix} \hat{i} + \begin{bmatrix} 0 \\ \tau_{xy} \\ \tau_{yy} \\ \tau_{xy} u_x + \tau_{yy} u_y + q_y \\ J_{y,s} \end{bmatrix} \hat{j} . \tag{4}$$

The viscous stresses are

$$\begin{aligned} \tau_{xx} &= 2\mu \frac{\partial u_x}{\partial x} - \frac{2}{3}\mu \left(\frac{\partial u_x}{\partial x} + \frac{\partial u_y}{\partial y} + \frac{u_y}{y} \right) , \\ \tau_{yy} &= 2\mu \frac{\partial u_y}{\partial y} - \frac{2}{3}\mu \left(\frac{\partial u_x}{\partial x} + \frac{\partial u_y}{\partial y} + \frac{u_y}{y} \right) , \\ \tau_{xy} &= \tau_{yx} = \mu \left(\frac{\partial u_x}{dy} + \frac{\partial u_y}{dx} \right) , \end{aligned} \tag{5}$$

where μ is the dynamic viscosity of the gas mixture. The viscous heat fluxes are

$$\begin{aligned} q_x &= k\frac{\partial T}{\partial x} + \sum_{s=\text{all}} J_{x,s} h_s \ , \\ q_y &= k\frac{\partial T}{\partial y} + \sum_{s=\text{all}} J_{y,s} h_s \ , \end{aligned} \tag{6}$$

where k is the thermal conductivity of the gas mixture, T is the static temperature, J_x and J_y are the species mass diffusion fluxes and h_s is the standard enthalpy of formation of species s.

The vector of source term Q on the right-hand side of the governing equation can be written as

$$Q = \begin{bmatrix} 0 \\ 0 \\ 0 \\ 0 \\ \dot{\omega_s} \end{bmatrix}, \tag{7}$$

where $\dot{\omega_s}$ is the production/loss rate of species s.

The evaluation of thermodynamic (specific heat, enthalpy and entropy) properties for the component species used polynomial curve fits with the database from the NASA CEA program [28]. The evaluation of thermal transport (viscosity and thermal conductivity) properties for the component species primarily used the curve fits in the same form as that used by the CEA program. When a particular species data was not available, Sutherland's three coefficient law (based on kinetic theory) [29] was used to calculate transport properties. It should be noted that other studies [5, 10, 13, 20, 21, 24] have incorporated the CHEMKIN code [30] to evaluate the thermodynamic and transport properties for each species. CHEMKIN used essentially the same thermodynamic database and only a slightly different fitting procedure from the CEA code by Gordon and McBride [28]. The state for the gas mixture was then calculated based on a mass fraction weighted sum of individual species for thermodynamic properties and using Wilke's mixing rule [31] for transport properties.

Fick's law, using mixture-averaged diffusion coefficients [32] is implemented to evaluate the species mass diffusion. The mixture-averaged diffusivity of species s is expressed as

$$D_s = \frac{1 - x_s}{\sum_{i \neq s}^{N} (x_i / \mathcal{D}_{si})} \ , \tag{8}$$

where x_s and x_i are the mole fractions of species s and i respectively, N represents the total number of species in the mixture, $\mathcal{D}_{si}$ is the binary diffusion coefficient for the species pair s and i and can be calculated from the CHEMKIN transport database [33] using the Chapman-Enskog relation [32].

A correction for calculated fluxes is performed in order to guarantee total mass conservation numerically (i.e., meet the requirement of the diffusion mass fluxes summing to zero) [34]. The species mass diffusion fluxes are thereby expressed as

$$\begin{aligned} J_{x,s} &= -\rho D_s \frac{\partial Y_s}{\partial x} - Y_s \sum_{i=\text{all}} \rho D_i \frac{\partial f_i}{\partial x} \ , \\ J_{y,s} &= -\rho D_s \frac{\partial Y_s}{\partial y} - Y_s \sum_{i=\text{all}} \rho D_i \frac{\partial f_i}{\partial y} \ . \end{aligned} \tag{9}$$

The mixture-averaged diffusion model has been proved to be accurate in predicting the laminar burning velocity of premixed methane/air and hydrogen/air flame compared to the full multicomponent diffusion model [35]. This diffusion model was also widely used in micro/mesoscale combustion simulations [5, 11, 36].

The solver uses operator-splitting to sequentially update the flow properties due to fluid dynamics (inviscid and viscous fluxes) and then the changes due to chemistry (combustion reactions). For the fluid dynamics computation, the cell-centred variables of pressure, temperature, velocity components and species mass fractions are reconstructed using a piecewise parabolic method as presented in Gollan and Jacobs [27] (PPM) at cell interfaces. Other flow quantities e.g. density and internal energy are then calculated from the thermochemical model. Based on the reconstructed values, the AUSM$^+$-up flux calculator [37] which has specifically been formulated to maintain accuracy at all speed regimes for compressible flow is used to compute the inviscid fluxes. The Gausss divergence theorem is applied to compute

the spatial derivatives at the centre of secondary cells (defined as the volume surrounding a primary-cell vertex). Then the vertex values are averaged to obtain a midface viscous flux. Finally, a quasi-steady state ODE solver is used for the finite-rate chemistry implementation to determine the chemical production and loss term $\dot{\omega}$. The details of these solver numerics can be found in [27].

It should be mentioned that in the low Mach number limit the standard density-based compressible code may have stability and accuracy problems [37–39]. This is because the large disparity in acoustic wave speeds and small-magnitude flow velocities renders the system considerably stiff. A large portion of studies in literature [9–11, 13, 21, 24] used the SIMPLE (Semi-implicit pressure linked equations) scheme (a pressure-based method originally developed for incompressible flows) [40] to avoid density-based compressible flow issues. Other studies [5] performed modifications to their compressible solvers downward to low Mach numbers through decomposing the pressure into two terms - thermodynamic pressure and hydrodynamic pressure. Our code, alternatively used the AUSM$^+$-up flux splitting scheme (proved to be reliable and effective for low Mach number compressible flows [37]) to solve this issue without modifying the governing equations.

Time-accurate and numerically stable solutions are obtained by using the explicit three-stage Runge-Kutta time-marching scheme and setting the Courant-Friedrichs-Lewy (*CFL*) number to a relatively low value to choose the simulation time step. Figure 2 shows the *total heat release rate* (*THRR*) evolution for a period of flame propagation time using different *CFL* numbers. The *THRR* is calculated by integrating the *HRR* over the whole computational domain:

$$THRR = \int_V HRR\, dV = -\int_V \sum_{s=\text{all}} \dot{\omega}_s h_s\, dV \ . \tag{10}$$

Results indicate that the *CFL* number of 0.45 is small enough for obtaining time-step-independent solutions and is thereby set in this study. Further increase of the *CFL* number could lead to difficulties in solving for the thermodynamic state of the gas mixture, owing to the relatively "loose" coupling between the gas-dynamic processes and the highly nonlinear

finite-rate chemical-kinetic processes under the current sequence of operations for the time-step update.

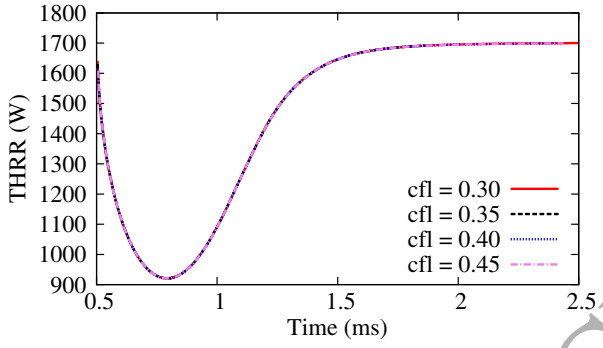

Figure 2: Effect of the *CFL* numbers on the *total heat release rate* (*THRR*) evolution for a period of flame propagation time.

In the following sections, the effect of some modelling choices on the micro-flame problem will be assessed, including grid refinements, boundary conditions, reaction schemes and flame ignition methods. In order to facilitate the discussion, it is necessary to establish a "baseline" case.

- Mesh density: 460×46 cells with the density of ∼0.013 mm. Detailed grid refinements were performed to ascertain that this was a suitable mesh density. These are discussed later.
- Boundary conditions (BC):
  - Inlet: The total temperature $T_0 = 300$ K, CH_4/air mixture equivalence ratio $\phi = 1.0$, and uniform mass flux $\dot{m}'' = 1.122$ kg/m^2/s ($\simeq 1$ m/s inflow velocity) are set. Under this condition, the flame is found to be stabilised roughly in the middle of the channel, which minimises the influence of the inflow/outflow boundary conditions on spatial derivatives of variables in the flame region to facilitate the grid refinement study.
  - Outlet: pressure $p = 1.01325 \times 10^5$ Pa is set for studying micro-flames at atmospheric conditions.

  - Wall: A hyperbolic tangent temperature profile ramping from 300 K to 1400 K is prescribed, as done in previous works [5, 20, 41].
  - Symmetry BC is not applied at the channel centreline, as also done by Pizza et al. [5] and Ayoobi et al. [17]. This allows any naturally occurring transverse oscillations to form. The symmetry BC at the centreline was found in past-work to suppress such behaviour.

- Domain fill conditions:
  - pressure equals outlet pressure
  - stagnation temperature equals inlet stagnation temperature
  - mass flux equals inlet mass flux

- Reaction scheme: DRM-19 [42]. It was pointed out by Marra et al. [43] that the ability of correctly reproducing the adiabatic flame temperature and extinction curve (in the equivalence ratio - residence time plane) was important for a proper choice of the chemistry scheme for studying combustion oscillations. The reaction scheme used in this study was found to be an accurate representation of the chemistry for heat release (determining the adiabatic flame temperature) and ignition delay (strongly correlated to flame ignition/extinction features) for CH_4-air combustion in [44]. Capturing heat release and ignition delay are of primary interest in transient microcombustion simulations.

- The ignition method of incorporating a short-lived "ignition-zone" (located between $0.75L$ - $0.8L$, in effect for the first 0.5 ms) is used, which is found to be the most efficient means to initiate the flame among three methods tested in this study.

Simulations in this study follow the "baseline" settings unless otherwise stated. This "baseline" is a case in which the flame, after initiation, is time-marched to its steady-state. The term "steady-state" is used to describe a stable flame which does not temporally change in its spatial location and the *THRR*. In Section 5, a case showing spatially oscillating flames,

in addition to the steady-state flame case, is also assessed for comparing different reaction schemes.

The criteria of the global mass and energy residuals (the maximum relative imbalance of the mass and energy equations over all computational cells) being below the threshold values noted in Equation 11 is applied to rigorously determine whether the flame has reached its steady-state:

$$\begin{aligned} Residual_{\,mass} &\leq 10^{-8} \\ Residual_{\,energy} &\leq 10^{-6} \end{aligned} \tag{11}$$

Figure 3 shows the temporal evolution of the global mass and energy residuals for the simulation of the "baseline" case. It can be found that the convergence criterion has been met after the simulation time t = 7.8 ms.

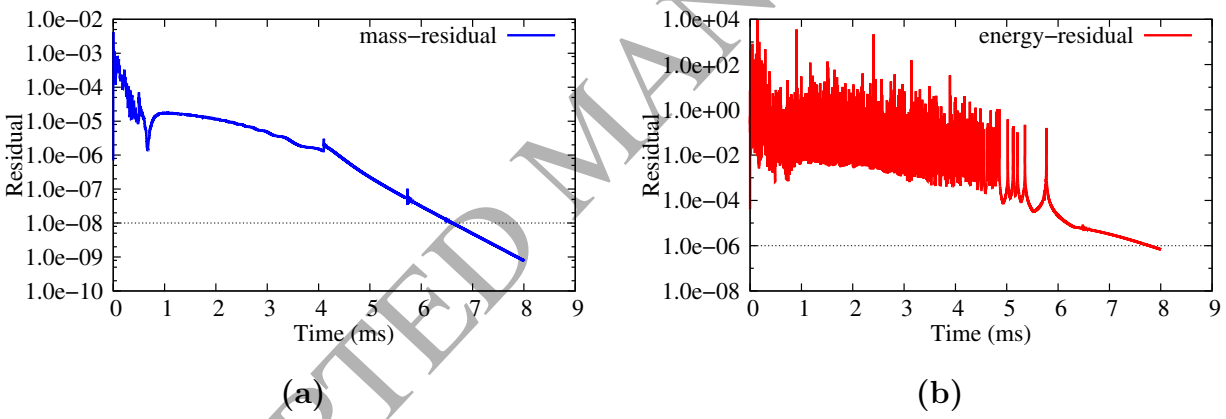

Figure 3: Global residuals for the mass (a) and energy (b) equation for the simulation of "baseline" case.

The simulations in this paper were performed in parallel using MPI with each simulation using 64 cores (2.6 GHz Intel Xeon processor) primarily on the Australian national supercomputing cluster [45]. The computational cost varies from case to case, some example numbers are listed in Section 5

3. Grid resolution

Grid convergence studies have not received a rigorous consideration for quantitative assessment in the microcombustion literature in general. The mesh density has typically been determined by visual observations of some of the variables (primarily the temperature along the flow direction) between successive mesh refinements or in some instances concluded on the basis that further refinement of the mesh produced no discernible change. What was deemed to be "discernible" is often unclear. Jejurkar and Mishra [14] performed a more rigorous method of computing the grid convergence index (GCI). The axial and radial reaction rate profiles were checked for their annular heat recirculating micro-combustor. This GCI method was originally proposed by Roache [46] and was more widely adopted in general CFD simulations including combustion simulations at conventional scale [47–49].

The method of grid convergence index (GCI) is based on the theory of Richardson Extrapolation [46]. As the grid is refined, the discrete solutions should approach the true value (exact solutions) asymptotically. The discrete solutions f on a mesh with spacing h can be related to the exact solutions f_{exact} via:

$$f = f_{exact} + g_1 h + g_2 h^2 + g_3 h^3 + ... \ , \tag{12}$$

where g_i is the coefficient of the i^{th} order error term and does not depend on the discretisation.

Equation (12) can be written for two uniform meshes with a grid refinement factor r

$$\begin{aligned} f_1 &= f_{exact} + g_1 h + g_2 h^2 + g_3 h^3 + ... \ , \\ f_2 &= f_{exact} + g_1 (rh) + g_2 (rh)^2 + g_3 (rh)^3 + ... \ , \end{aligned} \tag{13}$$

where 2 and 1 denote the coarse and finer mesh respectively.

Combining the two sub-equations in Equation (13) and neglecting the higher order error terms, the Richardson extrapolation estimate of the exact solution f_{exact} can be expressed as

$$f_{exact} \cong f_1 + \frac{f_1 - f_2}{r^{p_f} - 1} \ , \tag{14}$$

where p_f is the formal order of accuracy and equals to 2.0 with our second-order spatially accurate solver.

When solutions on three uniform meshes with a constant grid refinement factor are available, the convergence conditions of the system can be checked as suggested by Stern et al. [50]. There are three types of conditions possible:

$$\begin{aligned} &\text{(i)} \quad \text{Monotonic convergence} : 0 < R_c < 1 \\ &\text{(ii)} \quad \text{Oscillatory convergence} : R_c < 0 \\ &\text{(iii)} \quad \text{Divergence} : R_c > 1 \end{aligned} \tag{15}$$

where R_c is the convergence ratio and is written for the i^{th} mesh as

$$R_{c,i} = \frac{f_i - f_{i-1}}{f_{i+1} - f_i} . \tag{16}$$

For conditions of monotonic convergence, the observed order of accuracy $p_{o,i}$ can be extracted explicitly from three grid solutions after computing $R_{c,i}$ as above.

$$p_{o,i} = \ln(\frac{1}{R_{c,i}}) / \ln(r) . \tag{17}$$

Where, r is the grid refinement factor between successive meshes. The Grid Convergence Index (GCI) provides a uniform method for reporting grid refinement studies. The GCI indicates an error band on how far away the discrete solution is from the asymptotic value. For the grid refinement from coarser to finer mesh (i+1→i), the GCI can be written as

$$GCI_i = \frac{F_s}{r^p - 1} \left| \frac{f_{i+1} - f_i}{f_i} \right| , \tag{18}$$

where F_s is the factor of safety. Roache [46] has recommended $F_s = 3.0$ and $p = p_f$ for the minimal case of only two grid calculations while $F_s = 1.25$ and $p = p_{o,i}$ when three or more systematically-refined meshes are available. As suggested by Roache [46] and Oberkampf [51], for simple topologies of Cartesian meshes, grid refinement factors as small as $r = 1.1$ can be employed without significant effects from other error sources, such as machine round-off errors.

Therefore, a set of uniform meshes 125×13 (mesh-6), 162×17 (mesh-5), 210×22 (mesh-4), 273×27 (mesh-3), 354×36 (mesh-2) and 460×46 (mesh-1) with a grid refinement factor of ∼1.3 were used for our assessment of the micro-flame problem in this work. The roughly square cell size in the these meshes were 48.0, 37.0, 28.5, 22.0, 17.0 and 13.0 μm respectively. A uniform mesh (with no clustering of cells) was employed to preserve the same spatial accuracy over the entire domain as the flames simulated were moving through the channel until steady-state was achieved.

For the GCI calculation, the domain integrated variable *THRR* and peak values of the temperature and some important radicals/intermediates (methyl CH_3, hydroxyl OH, formyl HCO and carbon monoxide CO) mole fractions over the domain at different levels of mesh refinement were selected and compared for a steady-state flame.

The variable profiles along the channel centreline for different mesh levels are shown in Figure 4. When the mesh is refined from the coarsest level (mesh-6) to the finest level (mesh-1), solutions for all selected variables are clustered from visual observation. However, this "clustering" during the mesh refinement process has experienced three different stages:

- Oscillatory convergence: This condition occurs when the mesh is refined from the level 6 (125×13 cells) to level 3 (273×27 cells). As shown in Table 2, the calculated convergence ratios R_c are negative for the CH_3, OH and temperature peak for the grid refinement 6→5→4, and for the OH and temperature peak for the grid refinement 5→4→3 respectively. Moreover, even the flame location exhibits oscillatory convergence when the grid is refined, as can be seen in the domain-enlarged Figure 5. Without further grid-refinement, the grid-independent solutions cannot be attained at this oscillatory stage. This is also where the "visual" inspection method could face a potential pitfall. For example, if one accidentally selected mesh-6 (125×13 cells), mesh-5 (162×17 cells) and mesh-3 (273×27 cells) as the three meshes for a convergence study. It will be tempting to choose mesh-5 as being sufficient. However, this will be incorrect as this mesh is in the "oscillatory" convergence region as seen from Fig. 5, where the temperature and the CH_3 profiles show that mesh-4 (210×22) deviates from

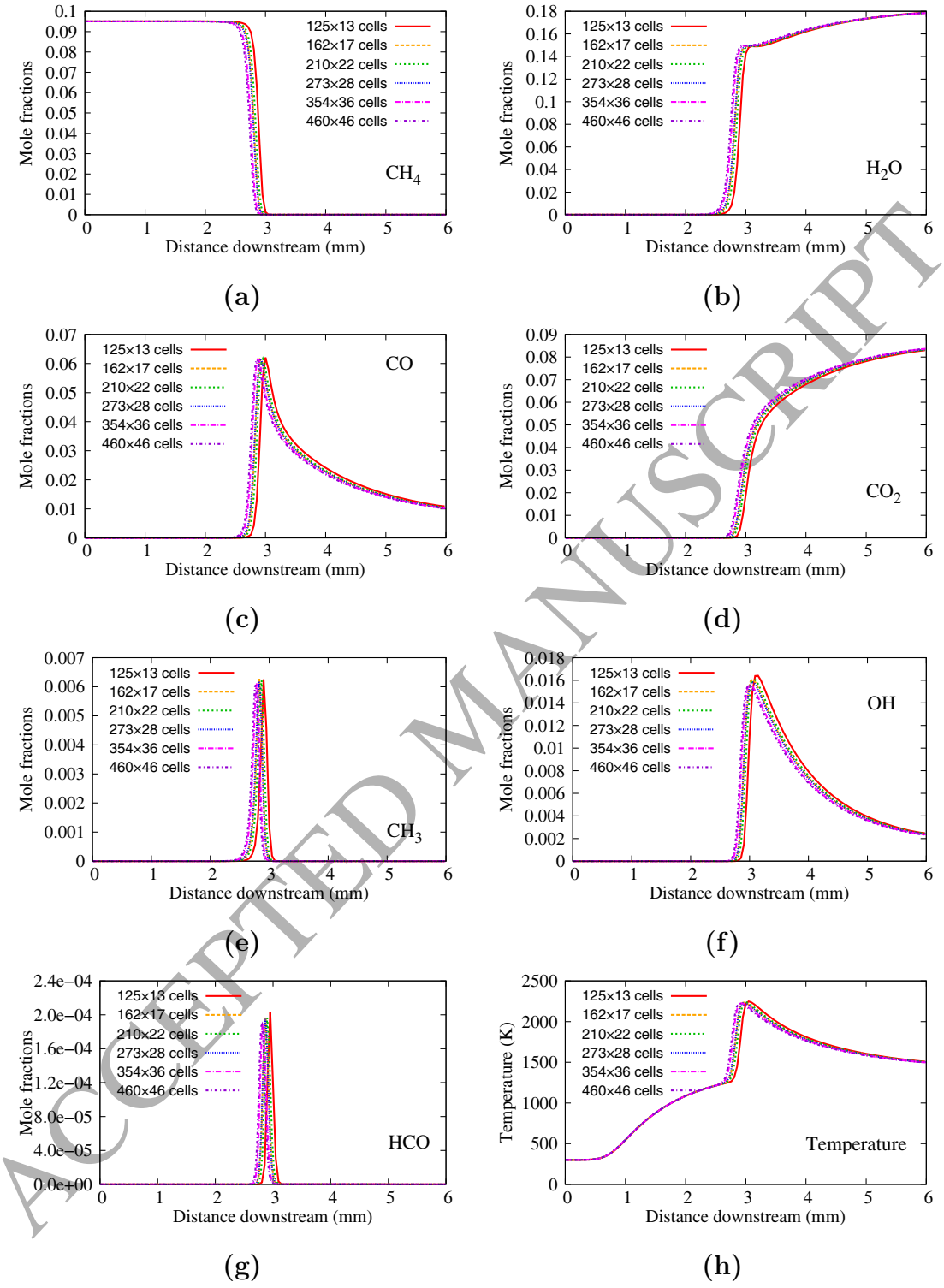

Figure 4: Profiles of temperature and species mole fractions along the channel centreline at different mesh levels for steady-state flames at t = 8.0 ms.

mesh-5 and mesh-3 in an oscillatory manner. Moreover, a statistically quantifiable error such as the GCI cannot be computed for these meshes. If the objective of the computational study is a temporally changing phenomenon (such as flame oscillations or other dynamic behaviour) then choosing such a grid, that is not converged properly even for a "steady" solution, would make it impossible to discern a "real" physical phenomenon from numerical artefacts.

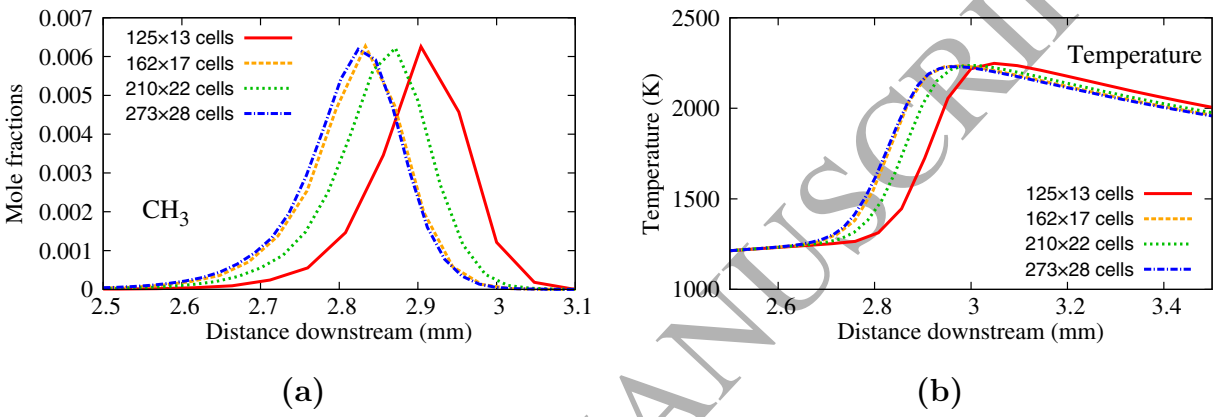

Figure 5: Grid refinement from the mesh-6 to mesh-3, showing oscillatory convergence ($R_c < 0$).

- Divergence: Upon further mesh refinement 4→3→2, the peak values of all selected species show divergence with the calculated convergence ratios $R_c > 1$, as indicated in Table 2. However, the domain integrated variable *THRR* shows good convergence behaviour (monotonic) with the convergence ratio $0 < R_c < 1$ and the observed order of accuracy $p_o = 2.35$ approaching the formal order of accuracy ($p_f = 2.0$). A domain-enlarged plot at this refinement stage is also shown in Figure 6.

- Monotonic convergence: As discussed earlier, discretisation errors due to truncation of the domain can only be quantitatively assessed when the solutions are monotonically converged. This condition has been achieved for the mesh refinement 3→2→1. As shown in Table 2, for all of the variables examined, the convergence ratios R_c are between 0 and 1. However, the variables that are examined on a "peak value" basis are found to have the observed order of accuracy (p_o) deviated from the formal order of

Table 2: Summary of the GCI calculation for selected variables on different mesh levels for steady-state flames at t = 8.0 ms.

Mesh		$X_{CH_3,max}$	$X_{OH,max}$	$X_{HCO,max}$	$X_{CO,max}$	T_{max} (K)	*THRR* (W)
6 (125 × 13)	f	6.254×10^{-3}	6.208×10^{-2}	2.035×10^{-4}	1.641×10^{-2}	2248.37	1690.09
5 (162 × 17)	f	6.267×10^{-3}	6.143×10^{-2}	1.972×10^{-4}	1.606×10^{-2}	2235.12	1697.86
	R_c†	-4.07	-0.34	0.09	0.02	-0.08	0.02
	p_o	-	-	9.18	15.60	-	14.14
4 (210 × 22)	f	6.217×10^{-3}	6.165×10^{-2}	1.966×10^{-4}	1.606×10^{-2}	2236.16	1698.05
	R_c†	0.58	-0.21	2.80	37.88	-6.10	28.26
	p_o	2.07	-	-	-	-	-
3 (273 × 27)	f	6.189×10^{-3}	6.160×10^{-2}	1.950×10^{-4}	1.584×10^{-2}	2229.85	1703.42
	R_c†	2.71	4.69	2.99	1.02	0.99	0.54
	p_o	-	-	-	-	0.02	2.35
2 (354 × 36)	f	6.112×10^{-3}	6.139×10^{-2}	1.903×10^{-4}	1.562×10^{-2}	2223.59	1706.32
	R_c	0.67	0.35	0.35	0.37	0.54	0.59
	p_o‡	1.50	4.04	3.97	3.80	2.38	1.99
	GCI (%)	3.27	0.63	4.51	2.56	0.51	0.31
1 (460 × 46)	f	6.060×10^{-3}	6.131×10^{-2}	1.886×10^{-4}	1.554×10^{-2}	2220.23	1708.04
	GCI (%)∗	2.23	0.22	1.60	0.95	0.27	0.18

† If solutions show oscillation ($R_c < 0$) or divergence ($R_c > 1$), the observed order of accuracy p_o cannot be calculated (leading to either natural logarithms of negative numbers or negative values of p_o, according to Equation (17)).

‡ If the calculated observed order of accuracy p_o is larger than the formal order of accuracy p_f, an order of accuracy $p = p_f = 2.0$ will be used instead of the p_o for calculating the GCI.

∗ GCI calculation on mesh-1 shares the same R_c and p_o on mesh-2.

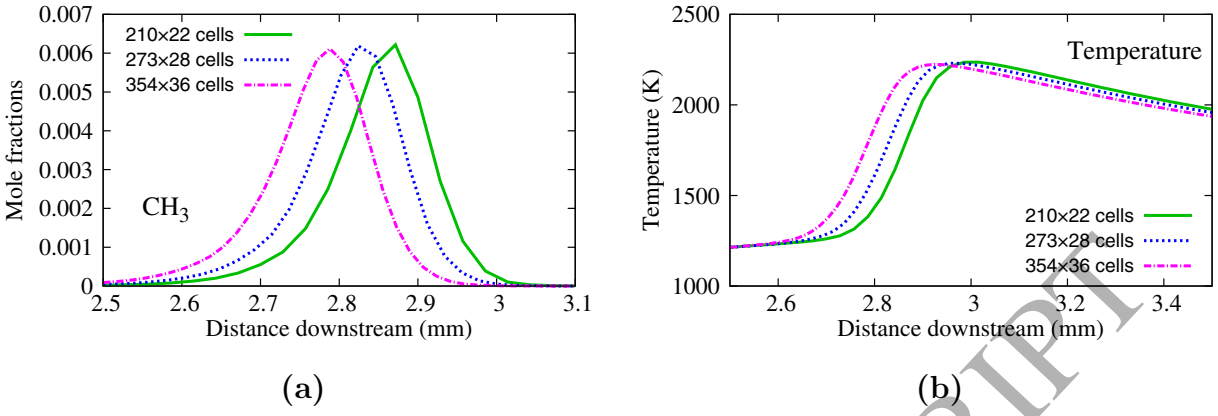

Figure 6: Grid refinement from the mesh-4 to mesh-2, showing divergence ($R_c > 1$).

accuracy ($p_f = 2.0$). The only domain integrated variable ($THRR$) matches the formal order of accuracy. This is because the spatially local variables are more "sensitive" to the mesh grading, while the domain integrated one which is globally evaluated over the whole computationally domain is easier to attain well behaviours during mesh refinements. For the calculated p_o larger than the p_f, an order of accuracy $p = p_f = 2.0$ is used for calculating the GCI to avoid underestimated discretisation errors. Results show that the computed GCI_2 and GCI_1 of all variables are below 5%, representing reasonably low discretisation errors for both the mesh-2 and mesh-1.

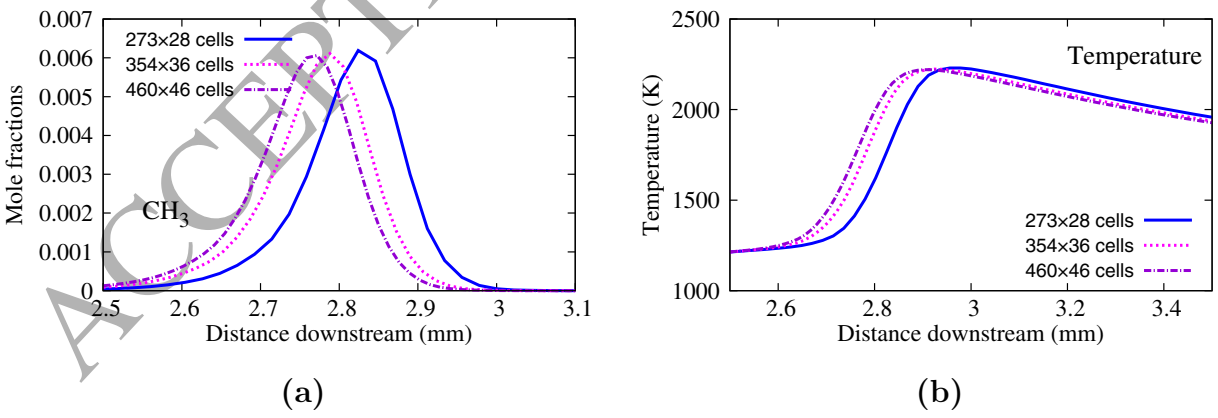

Figure 7: Grid refinement from the mesh-3 to mesh-1, showing monotonic convergence ($0 < R_c < 1$).

Therefore, the mesh size of 17 μm (mesh-2, 354×36 cells) is determined to be the maximum-sized mesh that can provide grid-independent solutions. This value is found to be slightly lower than many of the mesh densities used in the literature [5, 9, 10, 13, 17, 21, 24] (ranging from 19 to values larger than 50 μm). Since only a few of the past studies used the GCI method, visual observations of the solutions might have a less strict requirement on grid refinement. Moreover, the geometries/dimensions of the domain, reaction schemes used and spatial accuracy of the solver (for example, higher order schemes could allow for coarser mesh density to maintain the spatial accuracy [5, 20]) are also considered to be factors which affect the required mesh densities. However, the main point here is that the GCI method used in this paper is a proper way to quantify the discretisation errors during the mesh refinement process. It gives the confidence that the data presented by the authors are within the 5% error band compared to the exact solutions (Richardson extrapolated values).

In this work, all the results in the other sections are obtained in a conservative means of using the finest grid (460×46 cells, cell size of 13 μm). We chose this even though the GCI study showed that this is not strictly necessary, in order to minimize the influence of numerical error due to mesh density when investigating the other modelling choices.

4. Considerations on boundary conditions

In this section, we discuss our considerations on setting appropriate boundary conditions. Figure 8 shows the overview of the chosen boundary conditions for the modelling of combustion in a planar micro-channel.

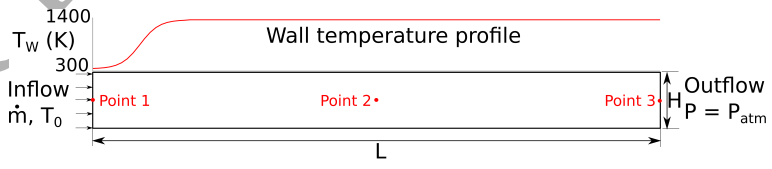

Figure 8: Boundary conditions used for the micro-channel and three monitored points for the comparison of two types of mass flux inflow boundary conditions.

A prescribed hyperbolic tangent wall temperature profile was first experimentally applied by Maruta et al. [52] and then became a typical wall boundary condition in transient micro-

combustion simulations [5, 20, 41]). The settings in literature can be viewed as a common method for simulating a decoupled heat transfer mechanism between the gas and solid wall. Since this paper focuses on the effect of modelling choices on the gas-phase combustion, we follow this setting to use a no-slip wall BC with a prescribed temperature distribution (to mimic the heat recirculation via wall conduction) as a baseline. The wall temperature ramps from the mixture inlet temperature of 300 K to a high temperature at 1400 K over the initial 1 mm of the channel length according to a hyperbolic tangent function, and was maintained at this value for the remaining length of the combustor.

A solid heat transfer solver (considering the heat conduction in the solid walls with both the convective and radiative heat transfer at the combustor outer surface) that is tightly coupled with our fluid solver has been newly developed and verified [53]. In future works for studying the performance of a "real" combustor, e.g. the transient thermal response of the walls to the flame propagation, time-accurate simulations can be conducted in a more complex manner accounting for the conjugate heat transfer at the fluid-solid interface.

At the outlet, the conditions are set to be atmospheric using a very well-established fixed pressure outflow BC (which was adopted in many past studies [5, 9, 10, 13, 14, 17–19, 21, 24, 41]). The pressure is set at 1.01325×10^5 Pa, while zero Neumann boundary conditions are imposed for the rest of the variables.

Although the symmetry boundary condition at the channel centreline was widely used in literature [9, 10, 13, 26, 54], steady and unsteady asymmetric flames in a full narrow channel were also reported in both experimental [55] and numerical studies [5, 17, 19, 26, 54]. In order to capture asymmetric features of the flame, all simulations need to be performed for a full channel without the symmetry assumption imposed.

For the inlet boundary, most of the past studies specified velocity profiles (either uniform [5, 9, 10, 13, 14, 21, 24] or fully developed [10, 11, 13, 20]) as well as the static temperature. However, it has been pointed out that the velocity inlet boundary condition is intended for incompressible flows [56, 57], while its use in compressible flows might lead to non-physical phenomena such as the stagnation conditions becoming very large or very small [57]. For compressible flows, two classes of inflow boundary conditions can be applied.

For the reservoir-type inflow BC, the total pressure and total temperature are prescribed to fix the stagnation condition [56, 57]. Our previous simulations [18] adopted this type of reservoir inflow BC to study the flame dynamics. Alternatively, one can also prescribe the total temperature and mass flux across the boundary and leave the total pressure to be self-adjusted, which is called the mass flow inlet boundary condition [57]. For the simulation of micro-flame problems, matching a prescribed mass flow flux is more "realistic" than matching the total pressure of the inflow stream, since the mass flow rate is usually regulated in experimental studies (e.g. via mass flow controllers).

In this work, two types of inflow mass flux boundary conditions have been applied and compared, in both of which, the gas total temperature (T_0), mass fractions of incoming species and a uniform mass flux ($\dot{m}''$) across the boundary are specified. However, other variables (velocity, static pressure and temperature, etc.) are calculated and set in two different means:

- BC-typical: A typical type of mass flow inlet boundary condition analogous to that used in the commercial CFD package FLUENT [57] was first tested. In this boundary condition, the static pressure p at the boundary is extrapolated from the cells inside the interface. Using the ideal gas law

$$p = \rho R T \tag{19}$$

where R is the gas constant of the inlet mixture, the velocity u can be related to the gas temperature T via

$$u = \frac{\dot{m}''}{\rho} = \dot{m}'' \frac{RT}{p} \tag{20}$$

The energy balance equation at the boundary can be written as

$$h_0(T_0) = h(T) + \frac{1}{2}u^2, \tag{21}$$

where h_0 and h are the total enthalpy at stagnation conditions and the enthalpy at the temperature of T respectively. Using the secant method for root-finding, Equation (21) can be solved to obtain the static temperature T.

- BC-NSCBC: A Navier-Stokes Characteristic boundary condition (NSCBC) based on the characteristic wave relations [58] was applied. This type of inflow BC is capable of dealing with numerical instabilities caused by acoustic waves propagating in the computational domain. Miyata et al. [20] had used a similar boundary condition from the NSCBC family for their direct numerical simulations (DNS) of micro-combustion (although the velocity profile was prescribed rather than the mass flux).

  In the NSCBC boundary condition, the amplitude variation of the outgoing sound wave from the characteristic analysis of the Navier-Stokes equations can be written as

$$L_{u-c} = (u - c)(\frac{\partial p}{\partial x} - \rho c \frac{\partial u}{\partial x}) \tag{22}$$

  where c is the local sound speed and $(u - c)$ represents the velocity of sound wave moving in the negative x directions (upstream-propagating).

  The entropy wave and the incoming sound wave (downstream-propagating) are then decoupled from the Local one-dimensional inviscid (LODI) relations [58] and can be expressed as

$$L_{entropy} = (1 - M_a)/(\frac{1}{\gamma - 1} + M_a) L_{u-c} \tag{23}$$

$$L_{u+c} = \frac{(M_a - 1)[M_a(\gamma - 1) - 1]}{(M_a + 1)[M_a(\gamma - 1) + 1]} L_{u-c} \tag{24}$$

  where M_a and γ are the local Mach number and heat capacity ratio respectively. According to the LODI relations, the time variation of the density is related to the amplitude variations of these three waves

$$\frac{\partial \rho}{\partial t} + \frac{1}{c^2}[L_{entropy} + \frac{1}{2}(L_{u-c} + L_{u+c})] = 0. \tag{25}$$

The updated change in the gas density ρ at each time step is used to compute the velocity u based on the specified mass flux $\dot{m}''$ via Equation (20). The same energy balance equation (Equation (21)) is solved using the secant root-finding method to evaluate the static temperature T. Finally, the static pressure p is obtained based on the ideal gas law (Equation (19)).

In order to make comparisons between the two types of mass flux inflow BC, three points at the centreline of the computational domain were selected to monitor the temporal variation of pressure, temperature and velocity. The chosen points are located at the two ends (the interior cells adjacent to the inlet and outlet boundary) and at the centre of the channel (shown in Figure 8).

As shown in Figure 9, simulations using BC-NSCBC and BC-typical exhibit almost the same behaviour for the temporal variations of variables. At the very start of the simulation, owing to the drastic change in the flow temperature and density, a considerable amount of acoustic waves are generated that propagate back and forth within the channel, leading to large pressure and velocity oscillations at the inlet (point 1) and outlet (point 3) respectively, and even backflow at the middle of the channel (point 2, for the time between 0.065 and 0.1 ms). In less than 0.5 ms, these oscillations are gradually damped out. The pressure reaches its stable values rapidly while the temperature and velocity need a longer time to evolve during the process of the flame propagation. As the flame propagates from the ignition position ($0.75L$ - $0.80L$) to its at-rest location (around the middle of the channel), the temperature and velocity at point 2 then increase beyond those at point 3, and finally all variables asymptotically approach their steady state (details of the flame propagation process will be discussed in Section 6).

Cross-sectional profiles at steady state of the streamwise velocity (x-direction) are compared for the two boundary conditions in Figure 10 so that the effect on entrance length development can be examined. The velocity profiles are extracted at locations 1%, 2%, 4%, 8% and 16% of the channel length. For both types of inflow BC, an identical entrance length of 8% of the channel length is required for the flow to become fully developed beyond the

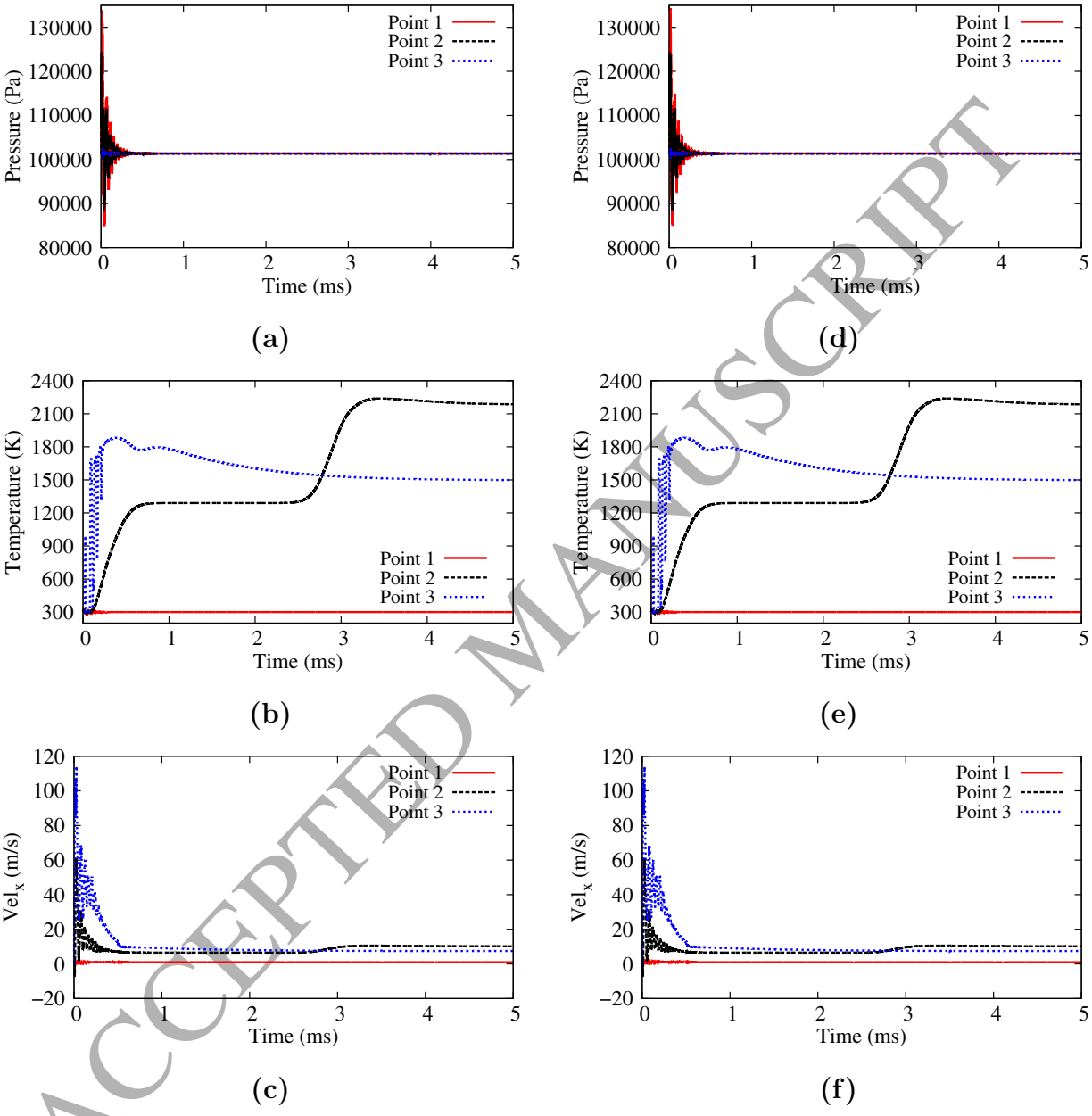

Figure 9: Temporal variation of pressure, temperature and velocity at three monitored points for the inflow boundary condition BC-typical ((a), (b) and (c)) and BC-NSCBC ((e), (d) and (f)) till 5 ms.

influence of entrance effects. The increased velocity at $x = 16\%$ of the channel length, is due to the thermal heating (from the hot wall and the flame) that the flow experiences which leads to a lowering of the density and consequently an increase in the velocity due to mass conservation.

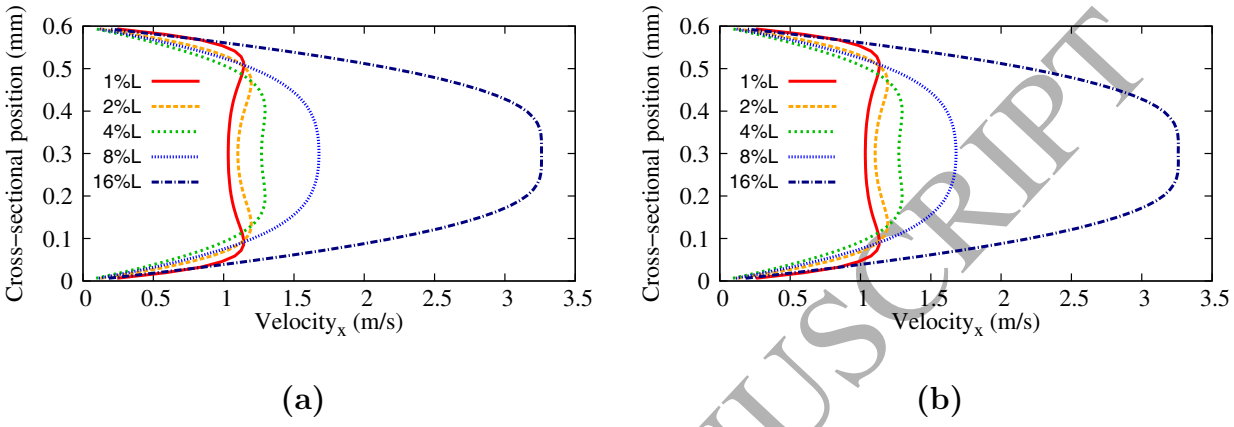

Figure 10: Cross-sectional x-velocity profiles at stream-wise locations of 1%, 2%, 4%, 8% and 16% of the channel length for the inflow boundary condition BC-typical (a) and BC-NSCBC (b), for steady-state solutions.

Since both types of inflow BC represent quite similar wave damping characteristics and the same steady-state solutions, while the BC-typical has a slightly lower computational cost (about 1.1 times faster) than that of the BC-NSCBC. The BC-typical is therefore selected and used for the remainder of this paper.

5. Reaction mechanisms

Combustion of hydrogen [5, 13, 14, 21, 24] or typical hydrocarbon fuels e.g. methane [10, 11, 17–20, 41, 59], propane [9] and syn-gas [60] were studied in past simulation works. Hydrogen has a higher energy density compared to hydrocarbons but it also suffers from severe problems of storage and transport [61]. This paper focuses on a safer and more reliable fuel, methane, which is the majority constituent of typical natural gas.

For the modelling of natural gas combustion, the reaction mechanism GRI-Mech [62] which involves 53 species and 325 elementary reactions is widely regarded as the most

complete scheme capable of providing the best predictability of combustion properties in the numerical combustion community. However, due to the limitation of computational cost, truncated or simplified reaction schemes were used in past micro-flame simulations [10, 11, 17–19, 59].

In this study, the 19-species and 84-reaction methane/air kinetics (DRM-19) [42] which was truncated from the full GRI-Mech chemistry was selected. Slavinskaya et al. [63] showed that the atmospheric laminar flame speeds calculated using the DRM-19 mechanism were in a very good agreement with both the full GRI-Mech scheme and experimental results. Moreover, this mechanism has also been proved to provide accurate modelling of ignition delay and heat release against experimental data [44]. Therefore, the DRM-19 as the subset of the full GRI-Mech scheme was considered to be a good compromise between saving computational costs and closely reproducing the main physical features of transient flames. Gauthier et al. [11] have also used this mechanism to study flame stabilisation problem in small channels.

Some other simplified reaction mechanisms which were commonly used for methane/air combustion were also examined and compared to the DRM-19 in this paper.

The Westbrook and Dryer two-step global reaction mechanism (WD-2) [64, 65] consists of two reactions, where the oxidation of CO to CO_2 is reversible:

$$\begin{aligned} &(i) \quad CH_4 + 1.5\,O_2 \rightarrow CO + 2\,H_2O \ , \\ &(ii) \quad CO + 0.5\,O_2 \rightleftharpoons CO_2 \ . \end{aligned} \tag{26}$$

Past simulations [59] used its reduced version of WD-1 only having a one-step irreversible reaction:

$$CH_4 + 2\,O_2 \rightarrow CO_2 + 2\,H_2O \ . \tag{27}$$

Another commonly used global reaction scheme by Jones and Lindstedt (JL-4) [66] consists of four reactions, where the third and fourth step are reversible:

$$
\begin{aligned}
&(i) \quad CH_4 + 0.5\,O_2 \rightarrow CO + 2\,H_2 \\
&(ii) \quad CH_4 + H_2O \rightarrow CO + 3\,H_2 \\
&(iii) \quad H_2 + 0.5\,O_2 \rightleftharpoons H_2O \\
&(iv) \quad CO + H_2O \rightleftharpoons CO_2 + H_2
\end{aligned}
\tag{28}
$$

The original article [66] only presented expressions for calculating the forward reaction rates of the four reactions. Methods for determining the reverse reaction rates of the step (iii) and (iv) can be found in references [67] and [68].

Smooke and Giovangigli [69] have proposed a skeletal methane combustion mechanism, involving 16 species and 25 reversible reactions. This well-understood mechanism was also frequently used in steady-state micro/mesoscale combustion simulations [10].

Simulation results with the above-mentioned reaction mechanisms (WD-2, JL-4, Smooke & Giovangigli and DRM-19) were compared for the solutions of a steady-state flame (using the same mesh density and the same inflow and boundary conditions as mentioned at the end of Section 2). Simulations with the GRI-Mech scheme was not performed due to the higher computational cost (approximately 4 times more expensive than the DRM-19).

Table 3 has summarised the steady-state *total heat release rate* ($THRR$) and combustion efficiency η for four reaction schemes. The combustion efficiency is defined as

$$
\eta = \frac{THRR}{\dot{m} \cdot Y_{CH_4} \cdot LHV_{CH_4}} \ , \tag{29}
$$

where $\dot{m}$, Y_{CH_4} and LHV_{CH_4} are the mixture mass flow rate, mass fraction and lower heating value of CH_4 respectively. Simulations with the different reaction mechanisms do not show too much difference in the $THRR$. The maximum difference is less than 5% (with respect to the DRM-19). The combustion efficiencies are all above 90% while the DRM-19 has the lowest degree of combustion completeness owing to many more species and reactions involved. Computational costs for simulations using different reaction schemes are also listed in Table 3.

Figure 11 shows the steady-state profiles of methane (CH_4), carbon monoxide (CO), car-

Table 3: Summary of the steady-state *total heat release rate*, combustion efficiency and computational costs for simulations using different reaction mechanisms with the same mesh density of 460×46 cells.

Mechanism	Species/ Reactions	Steady-state *THRR* (W)	Combustion efficiency η	Simulation time until steady-state (ms)	Wall clock time* per 1-ms simulation time (hrs/ms)
WD-2	5/2†	1788.09	96.2%	2.7	7.1
JL-4	7/4†	1809.74	97.4%	2.9	7.4
Smooke & Giovangigli	16/25†	1758.62	94.6%	3.1	24.2
DRM-19	22/84‡	1708.04	91.9%	7.8	43.2

* each simulation using 64 cores on the Australian national supercomputing cluster [45]

† including inert species N_2

‡ including inert species N_2, Ar and He

bon dioxide (CO_2) and temperature along the channel centreline for four reaction schemes. It was found that all four reaction mechanisms have led to different species and temperature distributions. Global mechanisms (WD-2 and JL-4) show large deviations in these profiles from the more detailed chemistry. Smooke & Giovangigli and DRM-19 mechanisms show similar profile shapes but different flame locations. This discrepancy can be attributed to the fact that the Smooke & Giovangigli predicts a higher burning velocity compared to the DRM-19 and thereby leads to a more upstream flame stabilisation location.

Apart from the above-discussed steady-state flame case, one unsteady flame case has also been examined for these reaction schemes. Figure 12 (a) shows the spatially oscillating flame within one oscillation cycle, which is obtained at a much lower inflow mass flux $\dot{m}'' = 0.2244$ kg/m^2/s (1/5 of the value for the "baseline" case), using the DRM-19 reaction scheme. The hyperbolic tangent wall temperature ramp is moved to the centre of the channel length, in order to avoid the flame interacting with the inflow boundary. This periodical flame

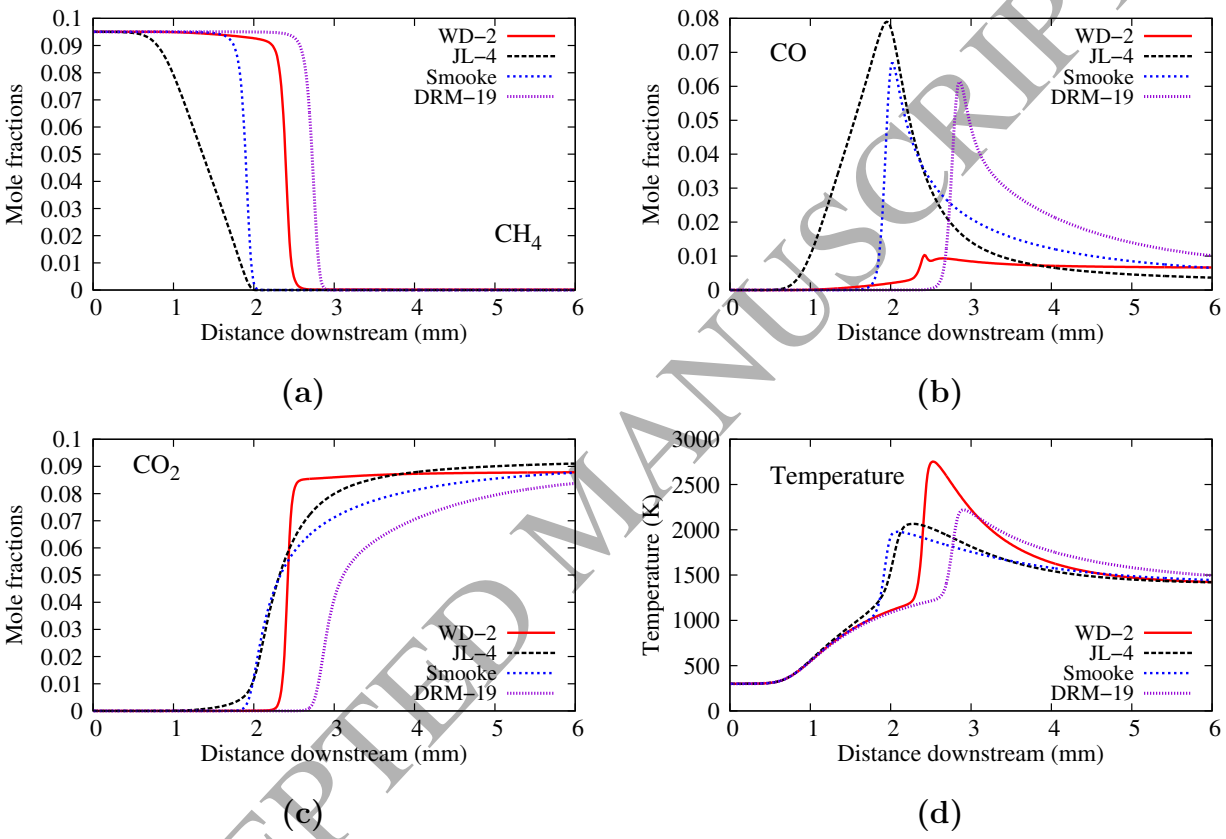

Figure 11: Profiles of CH_4, CO, CO_2 and temperature along the channel centreline for the reaction mechanism of WD-2, JL-4, Smooke & Giovangigli and DRM-19 for steady-state flames.

oscillation, is attributed to the competition between the flame propagation speed and the local flow velocity [22]. The flame propagation speed which is larger than the local flow velocity in the flame-upstream-moving phase, however, is weakened due to the large surface heat losses. During the phase where the flame propagates downstream, its propagation speed is lower than the local flow velocity. However, during this phase it also starts to get enhanced owing to the increased wall-preheating length.

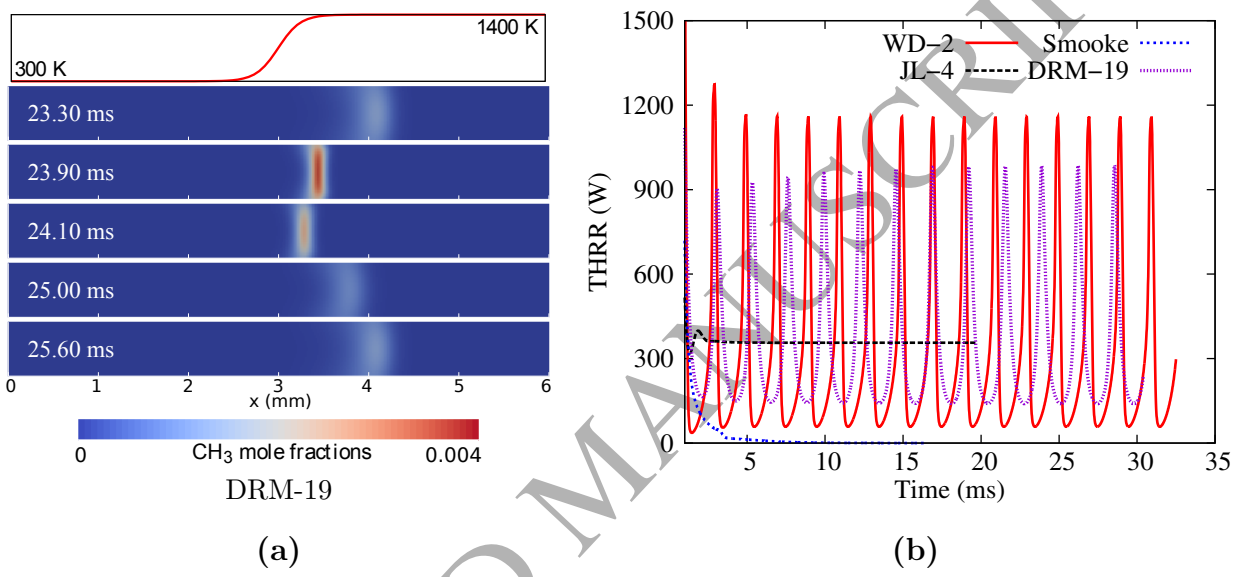

Figure 12: Spatially oscillating flames within one oscillation cycle, simulated using the DRM-19 reaction scheme (a), and The *THRR* versus the simulation time for the unsteady flame case, for various of reaction mechanisms (b).

The other three reaction mechanisms were also simulated at the same unsteady-flame condition. However, as shown in Figure 12 (b), the JL-4 shows flame stabilisation while the Smooke & Giovangigli eventually ends up with flame extinction. This can be explained by the fact that the JL-4 and Smooke & Giovangigli are not designed to predict the ignition delay which is strongly correlated to flame ignition/extinction features. For example, for the case of the Smooke & Giovangigli, the flame first propagates upstream (after ignition) and then gets weakened significantly owing to the "cold" walls. After that the flame is convected downstream by the flow and is eventually extinguished. Although the pre-heating length is

increased during the flame's downstream propagation, the mixture is found not capable of being re-ignited for this reaction mechanism.

Only the WD-2 shows periodically varying *THRR*. The oscillation frequency and peak-to-peak amplitude are moderately higher than the values for the DRM-19 (500 Hz vs 430 Hz, and 1100 W vs 846 W respectively). Although this mechanism has qualitatively captured this oscillating flame phenomenon, however, it always overestimates the flame temperature to a large extent as discussed earlier (shown in Figure 11) and is therefore not able to provide a reliable design answer for micro-combustors (especially when considering the temperature limit for mechanical failure of the combustor wall).

In summary, global reaction mechanisms of WD-2 and JL-4, and the skeletal scheme of Smooke & Giovangigli, were not able to appropriately predict either the steady-state flame structure, or the unsteady flame propagation. Therefore we do not recommend these for micro-flame simulations. On the other hand, the DRM-19 that is capable of accurately predicting laminar flame speeds [63], ignition delay and heat release [44], is recommended by the authors.

6. Ignition methods

Most of the transient micro-flame simulations in the literature focused on the dynamic behaviours after the flame was established rather than on the ignition process itself. The descriptions of the ignition process in the past works were only qualitative. This section aims to investigate various simulated ignition methods and provide some quantitative discussions.

There are several means used to initiate the flame in the literature. Nakamura et al. [41] used a steady-state flame as an initial solution to start the simulation. In Pizza et al.'s study of hydrogen combustion [5], the flame was auto-established starting from an initial "cold" flow condition via the heat transfer from the "hot" walls. Ayoobi and Schoegl [17] initiated the flame by a short-time artificial ignition event which introduced radicals into the channel at one cell upstream of the inlet. A high-temperature "patch" on the fluid zone was used in Wan et al.'s simulations to ignite their H_2/air mixture [24].

In present work, three types of ignition strategies that draw inspiration from the above references are used to initiate the flame:

- "Auto-ignition" - As the wall temperature is set high enough, the gas mixture is expected to be capable of being ignited automatically after adequate pre-heating time.
- "Heat-zone" - Heat addition (of 10^{10} W/m^3) within a small zone (0.3 mm $\times$ 0.6 mm, from $0.75L$ - $0.8L$) in the channel is prescribed for the first 0.5 ms of the simulation time to initiate the flame and then "switched-off" subsequently. The integrated heat addition over the special patch (1800 W) is quite close to the steady-state $THRR$ (1708 W). Lower values of the heat addition was found not able to ignite the flame within 0.5 ms while higher values could lead to large perturbations in the flow. In the source code implementation, this heat is added to the volumetric source term in the energy equation.
- "Ignition-zone" - An artificial rate-controlling temperature (set at 2000 K) is used within the same small zone as that for the "heat-zone" case to inflate the Arrhenius chemical reaction rates while keeping the thermodynamic temperature as per the flow condition. This zone was also in effect for the first 0.5 ms of the simulation time and then "switched-off" subsequently. It is a method of seeding the inflow with radicals similar to [17]. The seed composition then develops according to the inflow composition and reaction scheme. Since the seeding is controlled by a single parameter - the rate-controlling temperature, this method reduces the arbitrariness of seeding and conserves elemental mass. Under the current inflow condition, the set temperature of 2000 K is found to be the minimum value that can ignite the mixture within 0.5 ms (tested with the interval of 200 K, for example 1800 K is not able to establish the flame).

It should be mentioned that in "real" experiments, an electrode discharge or a torch/lighter is normally used to initiate the flame. In those ignition processes, a spark or an external flame delivers a sufficient amount of energy to heat the mixture inside the combustor to the threshold ignition temperature. In the sense of energy deposition, the numerical "heat-zone"

is more close to the experimental methods, although these physical ignition process can be much more "intrusive" (owing to the presence of the spark or the additional flame).

In the following discussions, the peak methyl radical (CH_3) mole fractions is chosen to represent the flame front location as CH_3 was found to be the key radical that controls the flame ignition and propagation via hydrogen abstraction reactions in the linear progression of CH_4 to CO_2. The propagation speed of the flame front S with respect to the local flow velocity u_x is defined as

$$S = \frac{dx_{CH_3}}{dt} - u_x \tag{30}$$

where dx_{CH_3}/dt is the moving velocity of the CH_3 concentration peak.

6.1. "Auto-ignition"

It is found that the "auto-ignition" method is not able to ignite the flame. Although the heat is transferred from the "hot" walls to the gas mixture, the short flow residence time does not allow generated radicals to accumulate to a necessary level which can trigger the combustion within the channel. As shown in Figure 13 (a), the *THRR* can only increase to a limited extent ($\sim$0.37 W) and then becomes flattened after the simulation time larger than 2 ms.

Therefore, a modified ignition strategy is used: the inflow mass flux is set at one tenth of the original value (from $\dot{m}'' = 1.122$ to 0.1122 kg/m^2/s) initially to increase the flow residence time until the the flame is ignited. After that, the $\dot{m}$ is adjusted back to the desired value.

Figure 14 plots the temporal evolution of the flame for the modified "auto-ignition" case. As the CH_4/air mixture flows through the channel, it gets heated by the "hot" walls. Consequently, CH_3 radicals are generated at the wall vicinity. With the increase of flow temperature, CH_3 radicals spread out more widely over the downstream portion of the channel. Then CH_3 radicals continue to accumulate and the peak moves near the channel exit due to the longest preheating length of the wall.

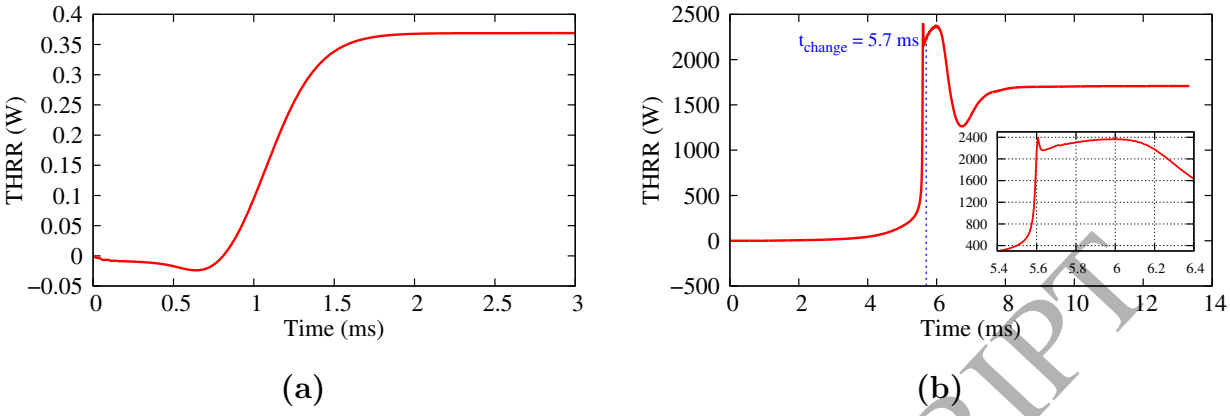

Figure 13: The *THRR* versus the simulation time for the cases using the original (a) and modified (b) "auto-ignition" method. For the modified method, the inflow mass flux $\dot{m}''$ is adjusted from 0.1122 to 1.122 kg/m^2/s at t$_{change}$ = 5.7 ms.

At t $\simeq$ 5.6 ms, a flame front is initiated and starts to propagate upstream within the channel. As shown in Figure 13 (b), the *THRR* increases rapidly within a short time and peaks at ∼2400 W. Then at t = 5.7 ms, the inflow mass flux is adjusted back to the original value of 1.122 kg/m^2/s. Since there is a delay before the high-velocity mixture flows through the channel, the flame continues to propagate and can reach a further upstream position than its final steady-state location. During this upstream-movement, the flame propagates quite fast, consuming the unburnt fuel rapidly with a high heat release rate.

At t $\simeq$ 6.3 ms, the flame reaches its most upstream location. After that, it gets weakened rapidly due to the large heat losses to the walls and shorter pre-heating length for the incoming mixture. As a result, the *THRR* experiences a drastic decrease (to a value of ∼1260 W at t = 6.7 ms), which leads to a highly decreased flame propagation speed. Subsequently, as the flame speed is lower than the local flow velocity, the flame is pushed downstream by the flow.

The downstream-moving flame moves much more slowly compared to the previous upstream-moving one. During this period, the *THRR* and flame propagation speed starts to increase again owing to the increasing pre-heating length for the reactants. Finally, as the flame speed is getting close to the local flow velocity, the flame approaches its final location. After

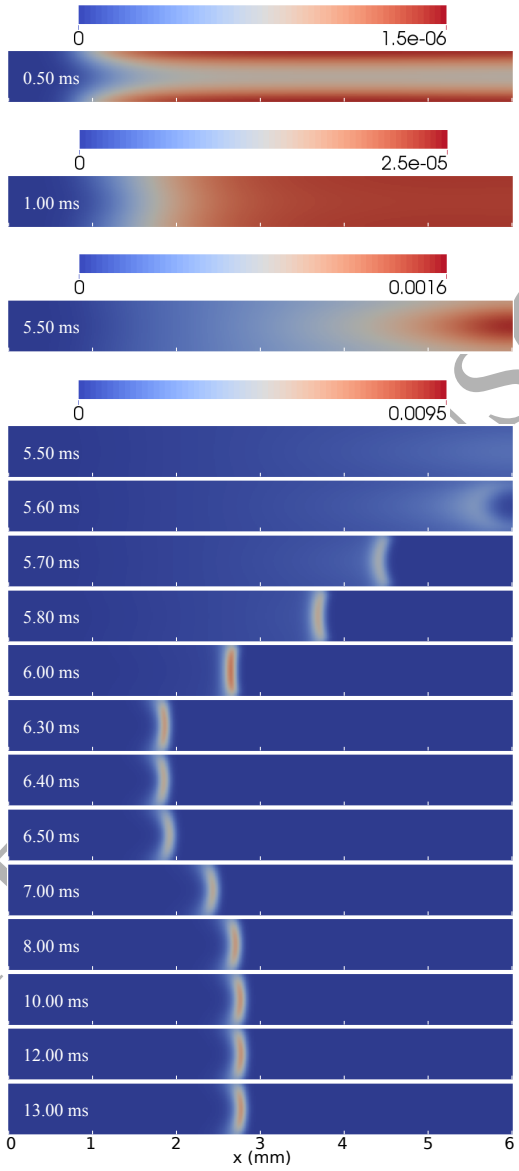

Figure 14: Temporal evolution of CH_3 mole fractions for the modified "auto-ignition" method.

t = 10 ms, there is no noticeable difference in the CH_3 mole fraction contours. The rigorous steady-state criterion (mass and energy residual) has eventually been met after t $\simeq$ 13 ms with a stable *THRR* value of 1708 W.

6.2. "Heat-zone"

In order to study the variation of the flame when using the special zones, the process of flame ignition and propagation was divided into three phases: ignition phase, flame bifurcation phase and flame propagation phase.

Figure 15 shows the ignition phase when using a "heat-zone". As a considerable amount of heat is added, CH_3 radicals are generated and accumulated within the zone gradually, and then retained near the walls at high temperature. Because of the artificial heat addition, chemical heat release as well as the the heat transfer from the "hot walls", the bulk flow temperature then goes beyond the wall temperature. Consequently, at t $\simeq$ 0.4 ms, CH_3 radicals start to move towards the channel centreline with a drastic increase in their concentrations. At t = 0.5 ms, the maximum CH_3 mole fractions and flow peak temperature reach the value of 2100 K and $\sim 5\times10^{-3}$ respectively, which is considered to mark the flame establishment. At the same time point, the artificial heating is switched off.

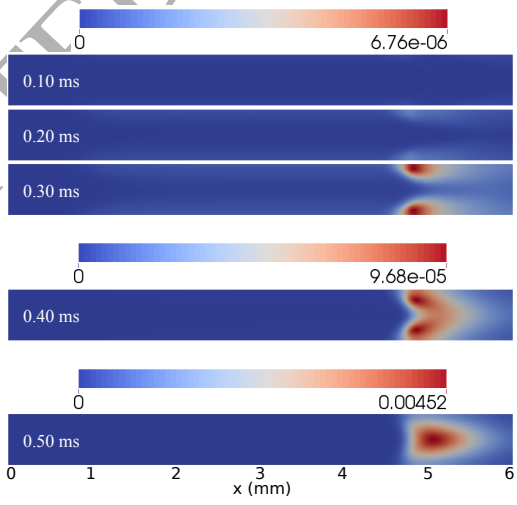

Figure 15: Temporal evolution of CH_3 mole fractions for the "heat-zone" method in the ignition phase.

After that, the flame is pushed a bit downstream owing to the absence of the "heat-zone". However, as the flame has already been ignited, its intensity increases drastically with a burst in the *THRR* (shown in Figure 16 (a)). Next, flame bifurcation starts to occur at t = 0.55 ms as shown in Figure 17. During this process, a bifurcated flame propagates downstream, consuming the unburned mixture at the tail of the channel while the main flame curved in the opposite direction propagates upstream. At t = 0.56 ms, the surface area of the two stretched flame fronts has been considerably increased, accompanied with a peak value of the *THRR* (∼5600 W). Subsequently, the bifurcated flame blows out, leading to a rapidly decreased *THRR* while the main flame changes its curvature and gets ready for the subsequent acceleration in the propagation phase.

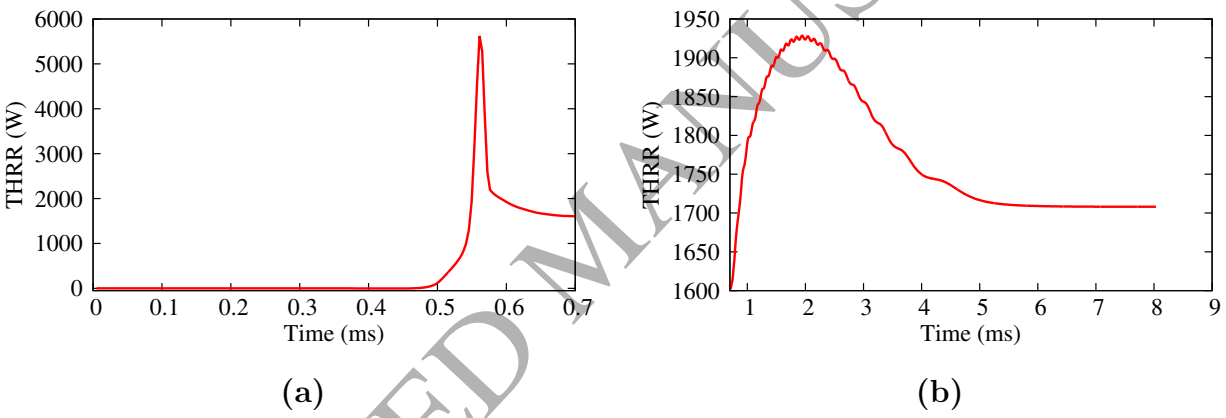

Figure 16: Temporal evolution of the *THRR* for the "heat-zone" method, for the simulation time from (a) 0 to 0.7 ms and (b) 0.7 to 9 ms.

Temporal evolution of the flame in the propagation phase is shown in Figure 18. The flame first propagates with quite a high speed, consuming the fuel rapidly with an increasing *THRR* (shown in Figure 16 (b)). However, the propagation speed decreases gradually as the flame moves more upstream. After t = 5.0 ms, the flame almost reaches its final location and there is no noticeable difference in the CH_3 mole fraction contours. Eventually, the flame evolves to its rigorous steady-state after t = 8.0 ms, with a stable *THRR* of 1708 W.

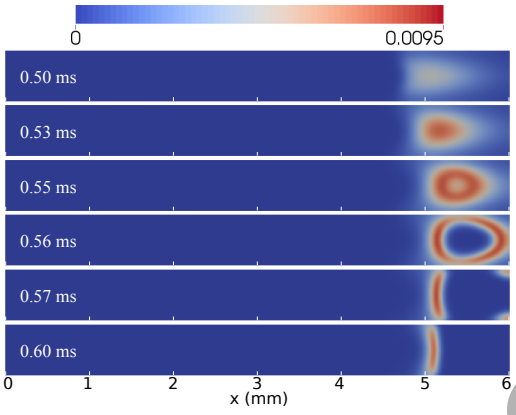

Figure 17: Temporal evolution of CH_3 mole fractions for the "heat-zone" method in the flame bifurcation phase.

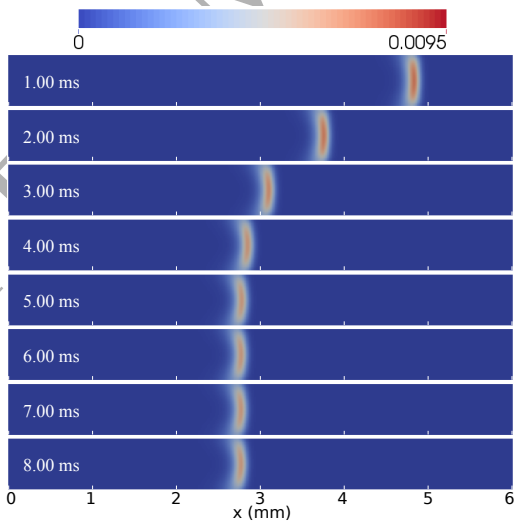

Figure 18: Temporal evolution of CH_3 mole fractions for the "heat-zone" method in the flame propagation phase.

6.3. "Ignition-zone"

The use of "ignition-zone" exhibits different flame ignition behaviours from the case using the "heat-zone" method. As shown in Figure 19, CH_3 radicals are immediately produced within the zone as the simulation starts. Since the artificially inflated rate-controlling temperature is set adequately high, the CH_3 mole fractions are at a much higher level (five orders of magnitude higher at t = 0.01 ms) than that for the initial CH_3 accumulation stage using the "heat-zone". However, as the flow suffers from large hydrodynamic oscillations owing to considerable back-and-forth propagating waves at the initial stage (as described in Section 4), the flame front also shows instabilities accompanied with repetitive flame bifurcations. This can be attributed to the fact that the mixture flows over the zone at quite high velocities (several tens of metres per second), leading to a low degree of combustion completeness. As a result, the remaining fuel flows further downstream and continues to burn, forming a secondary or tertiary flame front until it is blown out of the channel. The *THRR* (shown in Figure 20 (a)) also shows large oscillations during this period. As the initial hydrodynamic instabilities are gradually damped out, this repetitive flame bifurcations are ceased at $\simeq$ 2.8 ms.

Then after t = 0.5 ms, the rate-controlling temperature within the zone is re-adjusted from the inflated value (2000 K) to the actual thermodynamic temperature. Consequently, the *THRR* (shown in Figure 20 (b)) suffers from a sudden decrease from $\sim$2100 W to $\sim$1500 W. The flame also moves a bit downstream with a decreased propagation speed as shown in Figure 21. After t = 0.7 ms, the flame starts to propagate upstream again, exhibiting a similar propagation process as described in the "heat-zone" method. The *THRR* increases first and then decreases gently. A rigorous steady-state flame is achieved after t = 7.8 ms a final stable *THRR* value of 1708 W.

Figure 22 shows the profiles of the temperature and CH_4, CH_3 and CO mole fractions along the channel centreline for steady-state flames for three types of ignition strategies. It is found that different ignition methods have exactly the same steady-state solutions.

As shown earlier, the original "auto-ignition" method has difficulties of providing enough flow residence time to support reactions while the modified method which needs a reduced

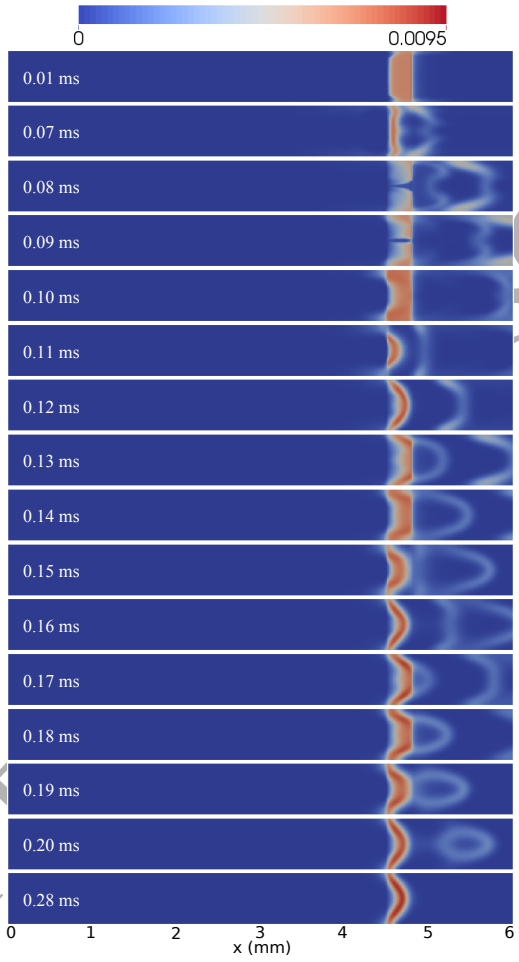

Figure 19: Temporal evolution of CH_3 mole fractions for the "ignition-zone" method in the ignition and flame bifurcation phase.

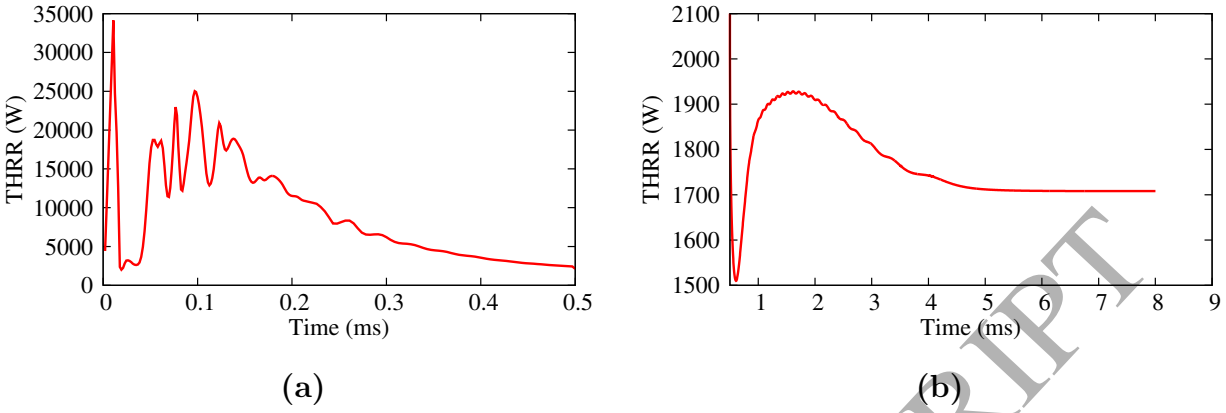

Figure 20: Temporal evolution of the *THRR* for the "ignition-zone" method, for the simulation time from (a) 0 to 0.5 ms and (b) 0.5 to 9 ms.

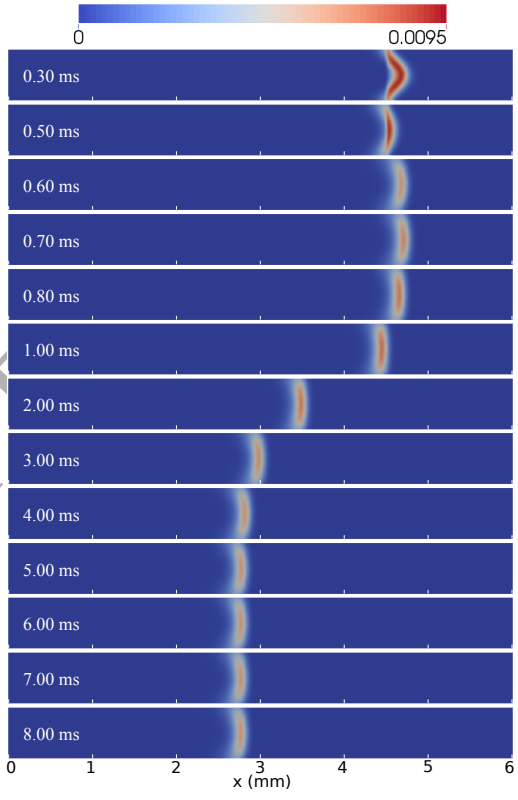

Figure 21: Temporal evolution of CH_3 mole fractions for the "ignition-zone" method in the flame propagation phase.

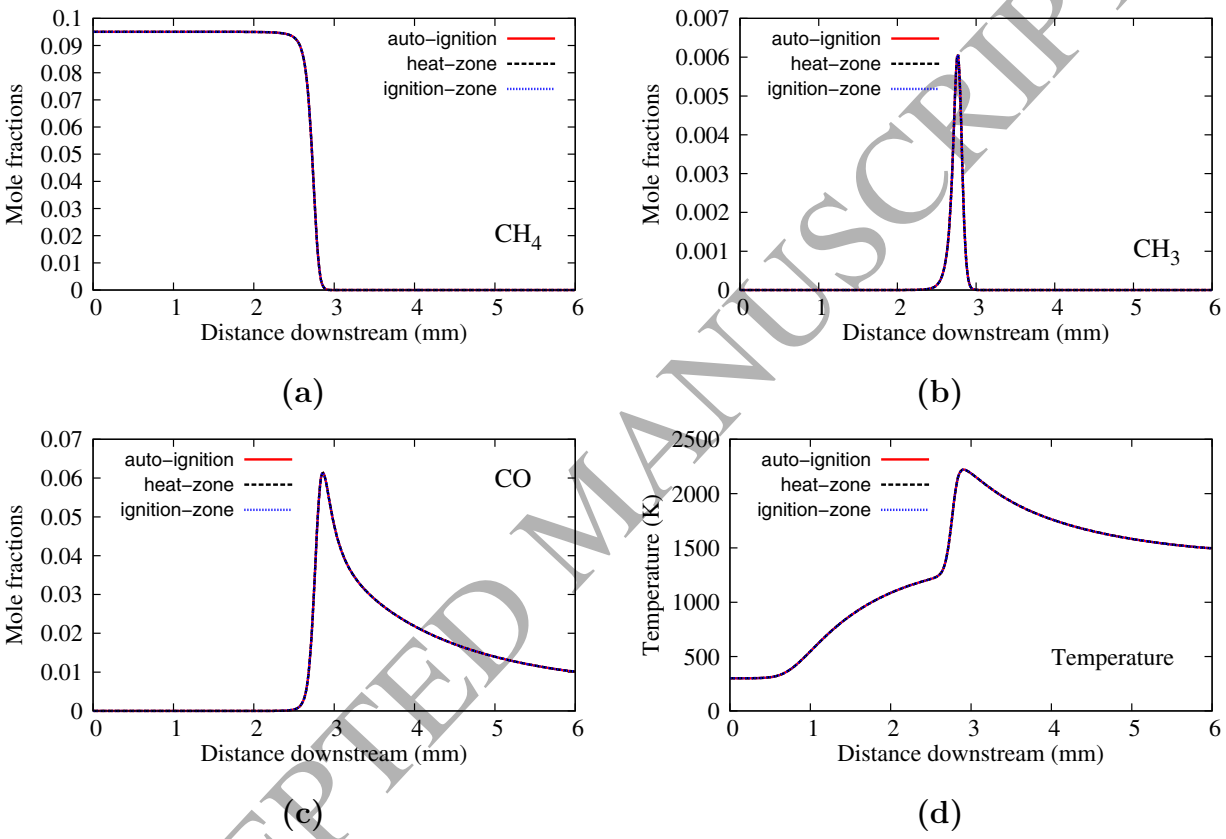

Figure 22: Steady-state profiles of the temperature and CH_4, CH_3 and CO mole fractions along the channel centreline for three types of ignition methods.

mass flow rate initially, requires much longer time for the key radicals to accumulate before the flame ignites compared to the "special zone" methods. Moreover, for future simulations with an even lower wall temperature or with a "real" conjugate heat transfer model that includes the heat conduction in the solid phase, the "auto-ignition" method might no longer be applicable.

When comparing two "special zone" methods, it is found that both the "heat-zone" and "ignition-zone" are capable of initiating the flame within a relatively short simulation time, without much pre-heating due to the hot wall. However, the use of the "heat-zone" method is found to exert larger perturbations on the flow field. Figure 23 shows the temporal variation of the pressure and x-velocity at the monitored point 2 (at the middle of the channel, as used in Section 4) around the time point of ceasing the "special zones" for two types of ignition methods. After t = 0.5 ms, the "switching-off" of the "heat-zone" results in considerably large acoustic oscillations owing to the sudden cease of the heat addition to the source term in the energy equation. As the heat addition (10^{10} W/m^3) used in simulations has already been optimised and is considered as the lowest value needed for igniting the flame within the zone-in-effect time, higher heat addition values are expected to have larger influences on the flow. On the other hand, only minor flow oscillations were observed for the case with the "ignition-zone". This is because this method only controls the rate-controlling temperature while there is no new term added to the governing equations and the thermodynamic temperature has not been artificially changed.

Therefore, among the three ignition strategies, the method of "ignition-zone" is recommended and will be used in the authors' future simulations. In the following sub-section, the independence of the zone duration time and zone locations on the steady-state solutions are examined.

6.4. Influence of the "ignition-zone" duration time and locations

In order to check the influence of the zone duration time (t_{effect}) on simulation results, one more case with t_{effect} = 1.0 ms has been tested. Figure 24 shows the *THRR* temporal variation for two cases with t_{effect} = 0.5 ms and t_{effect} = 1.0 ms. It can be found that

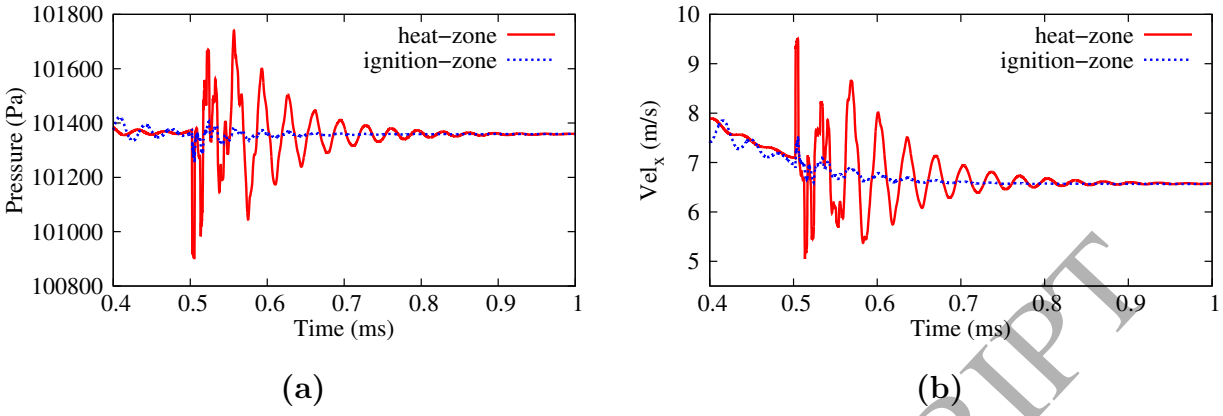

Figure 23: Temporal variation of the a) pressure and b) x-velocity at the monitored point 2 before and after the special "heat-zone" and "ignition-zone" switched off (from 0.4 to 1.0 ms).

different t_{effect} values only change the time point when the "switching-off" drop of the *THRR* occurs, while the *THRR* finally evolves to the same value (1708 W) with similar trends for both cases. From the temperature/species mole fraction profiles shown in Figure 25, there is also no difference found for the steady-state flame solutions.

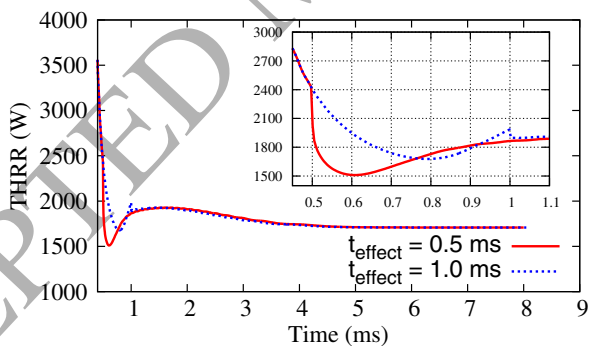

Figure 24: The *THRR* versus the simulation time for the "ignition-zone" duration time of t_{effect} = 0.5 ms and t_{effect} = 1.0 ms.

Another case with the "ignition-zone" located further upstream of (0.25-0.3)L (keeping other conditions unchanged) has also been simulated to investigate the influence of the zone location on the numerical solutions. As can be seen in Figure 26, the change of the zone location is found to result in no difference in the steady-state temperature and species mole

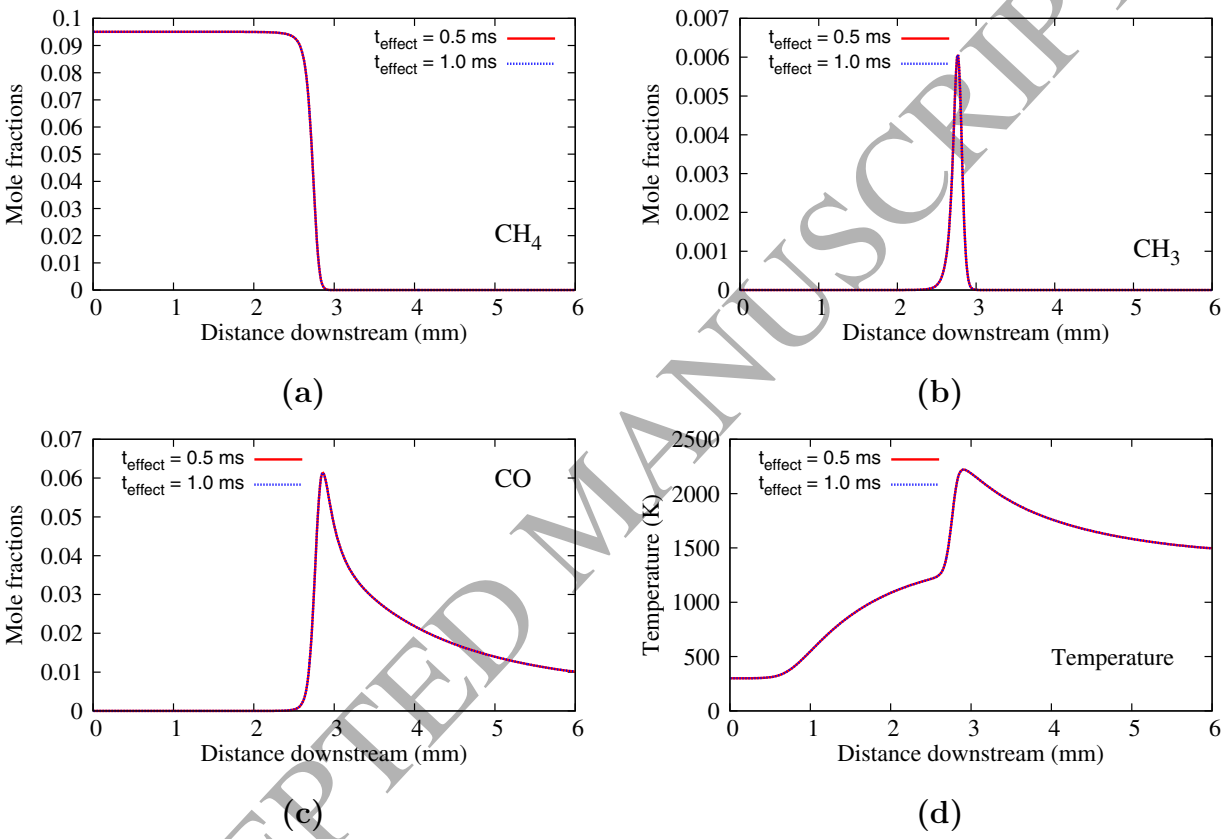

Figure 25: Steady-state profiles of the temperature and CH_4, CH_3 and CO mole fractions along the channel centreline for the "ignition-zone" duration time of t_{effect} = 0.5 ms and t_{effect} = 1.0 ms.

fraction profiles.

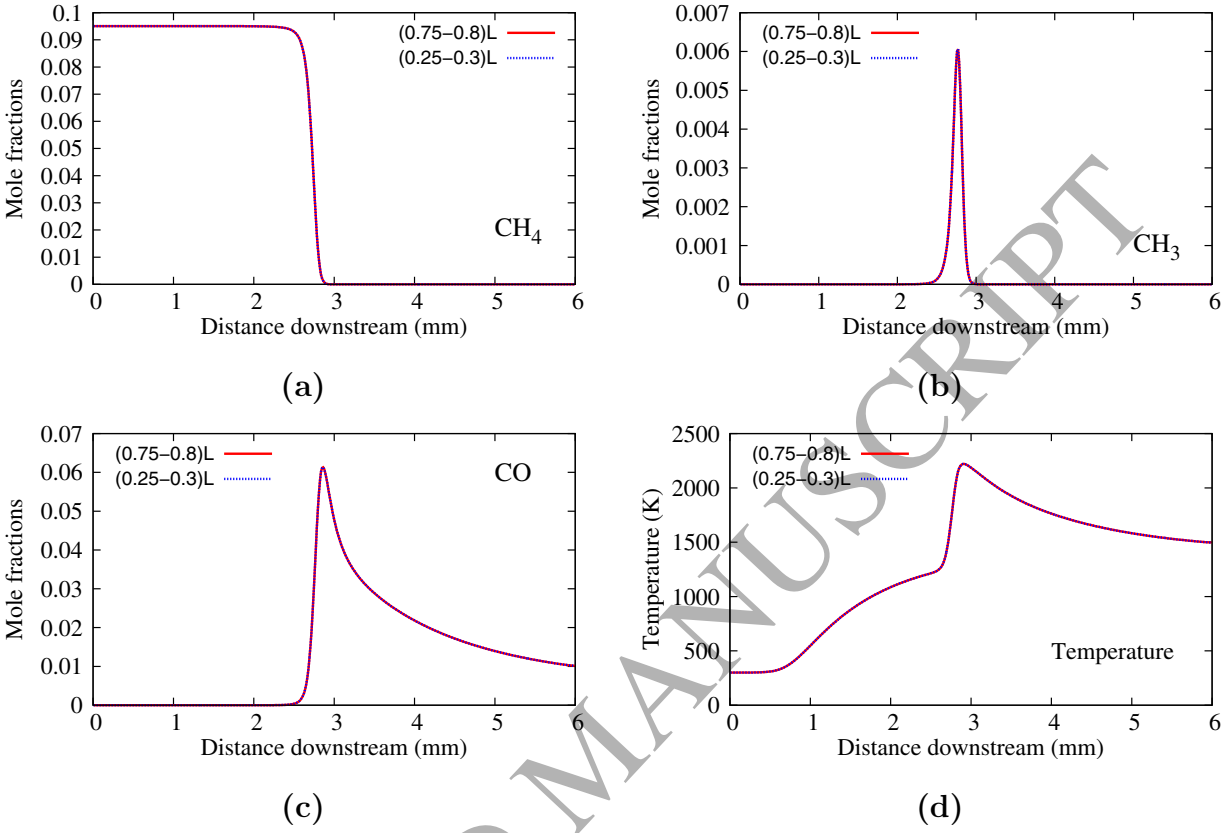

Figure 26: Steady-state profiles of the temperature and CH_4, CH_3 and CO mole fractions along the channel centreline for the "ignition-zone" at two locations of (0.75-0.8)L and (0.25-0.3)L.

Therefore, it can be confirmed that the "ignition-zone" is an effective and reliable method to initiate the flame. The steady-state results are independent of either the zone duration time or the zone locations.

7. Conclusions

This paper has developed a set of modelling techniques for simulating premixed methane/air flame propagation in a narrow channel. The authors' focus was mainly on the less well-established modelling choices, including grid refinements, boundary conditions, reaction schemes, and flame ignition methods. The main conclusions are drawn as follows:

1. A systematic grid refinement study was performed to examine the mesh requirement. The method of computing the grid convergence index (GCI) was used to estimate discretisation errors of the numerical solutions on each mesh levels. Results showed that the mesh size of 0.017 mm was small enough to afford reasonable and quantifiable numerical accuracy.
2. Two types of inflow mass flux boundary conditions have been tested. Both the BC-typical and BC-NSCBC showed the similar wave damping characteristics and identical steady-state solutions were attained. The BC-typical was selected owing to its slightly lower computational cost.
3. The reaction mechanism DRM-19 has been chosen for simulating the micro-flame problems as it was proved to provide accurate predictions of the laminar flame speeds, ignition delay and heat release in literature. Other methane/air combustion schemes which were used in past micro-flame simulations were also examined and showed deviations in numerical results from the DRM-19.
4. Three types of ignition methods ("auto-ignition", "heat-zone" and "ignition-zone") to initiate the flame were tested. Although the flames exhibited different ignition and propagation behaviours among three methods, the solutions were found to be identical when the steady-state was achieved. The method of "ignition-zone" was capable of igniting the flame within a short simulation time and was also found to exert small perturbations on the flow field. Moreover, simulation results were found independent of either the zone duration time or the zone locations. Therefore, the "ignition-zone" method has been considered as an effective and reliable tool and will be used for future simulations.

8. Acknowledgements

This research was undertaken with the assistance of resources from the National Computational Infrastructure (NCI) which is supported by the Australian Government and was supported under Australian Research Council's LIEF funding scheme (project number LE120100181).

References

[1] A. C. Fernandez-Pello, Micropower generation using combustion: Issues and approaches, Proceedings of the Combustion Institute 29 (1) (2002) 883–899.

[2] N. S. Kaisare, D. G. Vlachos, A review on microcombustion: Fundamentals, devices and applications, Progress in Energy and Combustion Science 38 (3) (2012) 321–359.

[3] C. J. Evans, D. C. Kyritsis, Operational regimes of rich methane and propane/oxygen flames in mesoscale non-adiabatic ducts, Proceedings of the Combustion Institute 32 (2) (2009) 3107–3114.

[4] X. Kang, A. Veeraragavan, Experimental investigation of flame stability limits of a mesoscale combustor with thermally orthotropic walls, Applied Thermal Engineering 85 (2015) 234–242.

[5] G. Pizza, C. E. Frouzakis, J. Mantzaras, A. G. Tomboulides, K. Boulouchos, Dynamics of premixed hydrogen/air flames in microchannels, Combustion and Flame 152 (3) (2008) 433–450.

[6] A. Fan, S. Minaev, E. Sereshchenko, R. Fursenko, S. Kumar, W. Liu, K. Maruta, Experimental and numerical investigations of flame pattern formations in a radial microchannel, Proceedings of the Combustion Institute 32 (2) (2009) 3059–3066.

[7] A. Veeraragavan, C. P. Cadou, Flame speed predictions in planar micro/mesoscale combustors with conjugate heat transfer, Combustion and Flame 158 (11) (2011) 2178–2187.

[8] A. Veeraragavan, On flame propagation in narrow channels with enhanced wall thermal conduction, Energy 93, Part 1 (2015) 631–640.

[9] D. Norton, D. Vlachos, A CFD study of propane/air microflame stability, Combustion and Flame 138 (1–2) (2004) 97–107.

[10] J. Li, S. Chou, W. Yang, Z. Li, A numerical study on premixed micro-combustion of CH_4/air mixture: Effects of combustor size, geometry and boundary conditions on flame temperature, Chemical Engineering Journal 150 (1) (2009) 213–222.

[11] G. P. Gauthier, G. M. G. Watson, J. M. Bergthorson, An evaluation of numerical models for temperature-stabilized CH_4/air flames in a small channel, Combustion Science and Technology 184 (6) (2012) 850–868.

[12] G. P. Gauthier, G. M. Watson, J. M. Bergthorson, Burning rates and temperatures of flames in excess–enthalpy burners: A numerical study of flame propagation in small heat–recirculating tubes, Combustion and Flame 161 (9) (2014) 2348–2360.

[13] J. Li, S. K. Chou, Z. W. Li, W. M. Yang, A comparative study of H_2-air premixed flame in micro combustors with different physical and boundary conditions, Combustion Theory and Modelling 12 (2) (2008) 325–347.

[14] S. Y. Jejurkar, D. Mishra, Flame stability studies in a hydrogen–air premixed flame annular microcombustor, International Journal of Hydrogen Energy 36 (12) (2011) 7326–7338.

[15] G. M. Watson, J. M. Bergthorson, The effect of chemical energy release on heat transfer from flames in small channels, Combustion and Flame 159 (3) (2012) 1239–1252.

[16] C. Jiménez, D. Fernández-Galisteo, V. N. Kurdyumov, DNS study of the propagation and flashback conditions of lean hydrogen–air flames in narrow channels: symmetric and non-symmetric solutions, International Journal of Hydrogen Energy 40 (36) (2015) 12541–12549.

[17] M. Ayoobi, I. Schoegl, Asymmetric methane/air flames in narrow channels, in: Fall Meeting of the Western States Section of The Combustion Institute, 2013.

[18] X. Kang, R. J. Gollan, P. A. Jacobs, A. Veeraragavan, Numerical simulations of premixed combustion in narrow channels, in: 19th Australasian Fluid Mechanics Conference, Melbourne, Australia, 2014.

[19] X. Kang, R. J. Gollan, P. A. Jacobs, A. Veeraragavan, Numerical simulation of premixed methane/air flame dynamics in narrow channels, in: Proceedings of the Australian Combustion Symposium, Melbourne, Australia, 2015.

[20] E. Miyata, N. Fukushima, Y. Naka, M. Shimura, M. Tanahashi, T. Miyauchi, Direct numerical simulation of micro combustion in a narrow circular channel with a detailed kinetic mechanism, Proceedings of the Combustion Institute 35 (3) (2015) 3421–3427.

[21] A. Nair, V. R. Kishore, S. Kumar, Dynamics of premixed hydrogen–air flames in microchannels with a wall temperature gradient, Combustion Science and Technology 187 (10) (2015) 1620–1637.

[22] X. Kang, R. J. Gollan, P. A. Jacobs, A. Veeraragavan, Suppression of instabilities in a premixed methane–air flame in a narrow channel via hydrogen/carbon monoxide addition, Combustion and Flame (2016), http://dx.doi.org/10.1016/j.combustflame.2016.07.003.

[23] A. Fan, J. Wan, Y. Liu, B. Pi, H. Yao, W. Liu, Effect of bluff body shape on the blow-off limit of hydrogen/air flame in a planar micro-combustor, Applied Thermal Engineering 62 (1) (2014) 13–19.

[24] J. Wan, A. Fan, H. Yao, W. Liu, Flame-anchoring mechanisms of a micro cavity-combustor for premixed H_2/air flame, Chemical Engineering Journal 275 (2015) 17–26.

[25] K. Maruta, Micro and mesoscale combustion, Proceedings of the Combustion Institute 33 (1) (2011) 125–150.

[26] V. N. Kurdyumov, Lewis number effect on the propagation of premixed flames in narrow adiabatic channels: Symmetric and non-symmetric flames and their linear stability analysis, Combustion and Flame 158 (7) (2011) 1307–1317.

[27] R. J. Gollan, P. A. Jacobs, About the formulation, verification and validation of the hypersonic flow solver Eilmer, International Journal for Numerical Methods in Fluids 73 (1) (2013) 19–57.

[28] B. J. McBride, S. Gordon, Computer program for calculation of complex chemical equilibrium compositions and applications. part 2: Users manual and program description, Technical Report 1311, NASA (1996).

[29] F. M. White, Viscous Fluid Flow, 3rd Edition, McGraw–Hill, New York, 2006.

[30] R. J. Kee, F. M. Rupley, J. A. Miller, The chemkin thermodynamic data base, Tech. Rep. No. SAND–8215B, Sandia National Laboratories (1992).

[31] C. R. Wilke, A viscosity equation for gas mixtures., Journal of Chemical Physics 18 (1950) 517–519.

[32] R. C. Reid, J. M. Prausnitz, B. E. Poling, The properties of gases and liquids, 4th Edition, McGraw–Hill, New York, 1987.

[33] R. J. Kee, G. Dixon-Lewis, J. Warnatz, M. E. Coltrin, J. A. Miller, A fortran computer code package for the evaluation of gas-phase multicomponent transport properties, Tech. Rep. No. SAND86–8246, Sandia National Laboratories (1996).

[34] K. Sutton, P. Gnoffo, Multi-component diffusion with application to computational aerothermodynamics, in: 7th AIAA/ASME Joint Thermophysics and Heat Transfer Conference, no. AIAA 98–2575, Albuquerque, NM, 1998.

[35] H. Bongers, L. P. H. D. Goey, The effect of simplified transport modeling on the burning velocity of laminar premixed flames, Combustion Science and Technology 175 (10) (2003) 1915–1928.

[36] D. Fernández-Galisteo, C. Jiménez, M. Sánchez-Sanz, V. N. Kurdyumov, The differential diffusion effect of the intermediate species on the stability of premixed flames propagating in microchannels, Combustion Theory and Modelling 18 (4-5) (2014) 582–605.

[37] M. Liou, A sequel to AUSM, part II: AUSM$^+$-up for all speeds, Journal of Computational Physics 214 (1) (2006) 137–170.

[38] E. Turkel, R. Radespiel, N. Kroll, Assessment of preconditioning methods for multidimensional aerodynamics, Computers & Fluids 26 (6) (1997) 613–634.

[39] A. Tomboulides, J. Lee, S. Orszag, Numerical simulation of low mach number reactive flows, Journal of Scientific Computing 12 (2) (1997) 139–167.

[40] S. Patankar, Numerical heat transfer and fluid flow, McGraw–Hill, New York, 1980.

[41] H. Nakamura, A. Fan, S. Minaev, E. Sereshchenko, R. Fursenko, Y. Tsuboi, K. Maruta, Bifurcations and negative propagation speeds of methane/air premixed flames with repetitive extinction and ignition in a heated microchannel, Combustion and Flame 159 (4) (2012) 1631–1643.

[42] A. Kazakov, M. Frenklach, Reduced Reaction Sets based on GRI–Mech 1.2, a 19–species reaction set, http://www.me.berkeley.edu/drm/, accessed April 2016.

[43] F. S. Marra, L. Acampora, E. Martelli, Non-linear response to periodic forcing of methane–air global and detailed kinetics in continuous stirred tank reactors close to extinction conditions, International Journal of Spray and Combustion Dynamics 7 (3) (2015) 175–208.

[44] B. O'Flaherty, Reducing the global warming potential of coal mine ventilation air by combustion in a free-piston engine, Ph.D. thesis, The University of Queensland (2012).

[45] National computing cluster Raijin, http://nci.org.au/nci–systems/, accessed April 2016.

[46] P. J. Roache, Verification and validation in computational science and engineering, Hermosapublishers, Albuquerque, New Mexico, 1998.

[47] J. Zhao, K. M. Isaac, Influence of geometry and heat release on counterflow diffusion flames: A navier-stokes model, International Journal of Computational Fluid Dynamics 8 (4) (1997) 287–298.

[48] Y. Jin, B. Shaw, Computational modeling of n-heptane droplet combustion in air-diluent environments under reduced-gravity, International Journal of Heat and Mass Transfer 53 (25–26) (2010) 5782–5791.

[49] D. Noriler, M. J. Hodapp, R. K. Decker, H. F. Meier, F. Meierhofer, U. Fritsching, Numerical simulation of flame spray pyrolysis process for nanoparticle productions: Effects of 2d and 3d approaches, in: Proceedings of the ASME 2014 4th Joint US-European Fluids Engineering Division Summer Meeting, Chicago, Illinois, USA, 2014.

[50] F. Stern, R. V. Wilson, H. W. Coleman, E. G. Paterson, Comprehensive approach to verification and validation of CFD simulations-part 1: Methodology and procedures, Journal of Fluids Engineering 123 (4) (2001) 793–802.

[51] W. L. Oberkampf, C. J. Roy, Verification and validation in scientific computing, Cambridge University Press, Cambridge, UK, 2010.

[52] K. Maruta, T. Kataoka, N. I. Kim, S. Minaev, R. Fursenko, Characteristics of combustion in a narrow channel with a temperature gradient, Proceedings of the Combustion Institute 30 (2) (2005) 2429–2436.

[53] A. Veeraragavan, J. Beri, R. J. Gollan, Use of the method of manufactured solutions for the verification of conjugate heat transfer solvers, Journal of Computational Physics 307 (2016) 308–320.

[54] V. N. Kurdyumov, G. Pizza, C. E. Frouzakis, J. Mantzaras, Dynamics of premixed flames in a narrow channel with a step-wise wall temperature, Combustion and Flame 156 (11) (2009) 2190–2200.

[55] U. Dogwiler, J. Mantzaras, P. Benz, B. Kaeppeli, R. Bombach, A. Arnold, Homogeneous ignition of methane–air mixtures over platinum: Comparison of measurements and detailed numerical predictions, Symposium (International) on Combustion 27 (2) (1998) 2275–2282.

[56] J. H. Ferziger, M. Perić, Computational Methods for Fluid Dynamics, 3rd Edition, Springer-Verlag Berlin Heidelberg GmbH, Berlin, 2002.

[57] Fluent Inc., Lebanon, NH, USA, Fluent 6.3 User's Guide (2006).

[58] T. J. Poinsot, S. Lele, Boundary conditions for direct simulations of compressible viscous flows, Journal of Computational Physics 101 (1) (1992) 104–129.

[59] N. Kaisare, D. Vlachos, Optimal reactor dimensions for homogeneous combustion in small channels, Catalysis Today 120 (1) (2007) 96–106.

[60] P. Boivin, C. Jiménez, A. L. Sánchez, F. A. Williams, A four-step reduced mechanism for syngas combustion, Combustion and Flame 158 (6) (2011) 1059–1063.

[61] A. Midilli, M. Ay, I. Dincer, M. Rosen, On hydrogen and hydrogen energy strategies: I: current status and needs, Renewable and Sustainable Energy Reviews 9 (3) (2005) 255–271.

[62] G. P. Smith, D. M. Golden, M. Frenklach, N. W. Moriarty, B. Eiteneer, M. Goldenberg, C. T. Bowman, R. K. Hanson, S. Song, W. C. Gardiner, Jr., V. V. Lissianski, Z. Qin, GRI–Mech 3.0, http://www.me.berkeley.edu/gri–mech/, accessed April 2016.

[63] N. Slavinskaya, M. Braun-Unkhoff, P. Frank, Reduced reaction mechanisms for methane and syngas combustion in gas turbines, Journal of Engineering for Gas Turbines and Power 130 (2) (2008) 021504–021504.

[64] F. Dryer, I. Glassman, High-temperature oxidation of CO and CH_4, Symposium (International) on Combustion 14 (1) (1973) 987–1003.

[65] C. K. Westbrook, F. L. Dryer, Simplified reaction mechanisms for the oxidation of hydrocarbon fuels in flames, Combustion Science and Technology 27 (1–2) (1981) 31–43.

[66] W. Jones, R. Lindstedt, Global reaction schemes for hydrocarbon combustion, Combustion and Flame 73 (3) (1988) 233–249.

[67] J. Andersen, C. L. Rasmussen, T. Giselsson, P. Glarborg, Global combustion mechanisms for use in CFD modeling under oxy-fuel conditions, Energy & Fuels 23 (3) (2009) 1379–1389.

[68] L. Wang, Z. Liu, S. Chen, C. Zheng, Comparison of different global combustion mechanisms under hot and diluted oxidation conditions, Combustion Science and Technology 184 (2) (2012) 259–276.

[69] M. Smoke, V. Giovangigli, Formulation of the premixed and nonpremixed test problems, in: Reduced Kinetic Mechanisms and Asymptotic Approximations for Methane–Air Flames, Vol. 384, Springer Berlin Heidelberg, 1991, pp. 1–28.